

Influence of Creep Compaction and Dilatancy on Earthquake Sequences and Slow Slip

Yuyun Yang¹ and Eric M Dunham²

¹The Chinese University of Hong Kong

²Stanford University

December 7, 2022

Abstract

Fluids influence fault zone strength and the occurrence of earthquakes, slow slip events, and aseismic slip. We introduce an earthquake sequence model with fault zone fluid transport, accounting for elastic, viscous, and plastic porosity evolution, with permeability having a power-law dependence on porosity. Fluids, sourced at a constant rate below the seismogenic zone, ascend along the fault. While the modeling is done for a vertical strike-slip fault with 2D antiplane shear deformation, the general behavior and processes are anticipated to apply also to subduction zones. The model produces large earthquakes in the seismogenic zone, whose recurrence interval is controlled in part by compaction-driven pressurization and weakening. The model also produces a complex sequence of slow slip events (SSEs) beneath the seismogenic zone. The SSEs are initiated by compaction-driven pressurization and weakening and stalled by dilatant suctions. Modeled SSE sequences include long-term events lasting from a few months to years and very rapid short-term events lasting for only a few days; slip is \sim 1-10 cm. Despite \sim 1-10 MPa pore pressure changes, porosity and permeability changes are small and hence fluid flux is relatively constant except in the immediate vicinity of slip fronts. This contrasts with alternative fault valving models that feature much larger changes in permeability from the evolution of pore connectivity. Our model demonstrates the important role that compaction and dilatancy have on fluid pressure and fault slip, with possible relevance to slow slip events in subduction zones and elsewhere.

Influence of Creep Compaction and Dilatancy on Earthquake Sequences and Slow Slip

Yuyun Yang^{1,2}, Eric M. Dunham^{1,3}

¹Institute for Computational and Mathematical Engineering, Stanford University

²Earth System Science Programme, Faculty of Science, The Chinese University of Hong Kong

³Department of Geophysics, Stanford University

Key Points:

- Fluid pressure changes from pore compaction and dilatancy influence slow slip events in our model
- Modeled slow slip events span long-term events lasting for months to years to rapid short-term events for a few days
- Earthquake recurrence interval is controlled in part by compaction-driven pressurization and weakening

1 Abstract

Fluids influence fault zone strength and the occurrence of earthquakes, slow slip events, and aseismic slip. We introduce an earthquake sequence model with fault zone fluid transport, accounting for elastic, viscous, and plastic porosity evolution, with permeability having a power-law dependence on porosity. Fluids, sourced at a constant rate below the seismogenic zone, ascend along the fault. While the modeling is done for a vertical strike-slip fault with 2D antiplane shear deformation, the general behavior and processes are anticipated to apply also to subduction zones. The model produces large earthquakes in the seismogenic zone, whose recurrence interval is controlled in part by compaction-driven pressurization and weakening. The model also produces a complex sequence of slow slip events (SSEs) beneath the seismogenic zone. The SSEs are initiated by compaction-driven pressurization and weakening and stalled by dilatant suctions. Modeled SSE sequences include long-term events lasting from a few months to years and very rapid short-term events lasting for only a few days; slip is \sim 1-10 cm. Despite \sim 1-10 MPa pore pressure changes, porosity and permeability changes are small and hence fluid flux is relatively constant except in the immediate vicinity of slip fronts. This contrasts with alternative fault valving models that feature much larger changes in permeability from the evolution of pore connectivity. Our model demonstrates the important role that compaction and dilatancy have on fluid pressure and fault slip, with possible relevance to slow slip events in subduction zones and elsewhere.

Plain Language Summary

Water in the crust plays an important role in controlling the strength of fault zones and frictional sliding, which manifest as earthquakes and slow slip events that do not produce ground shaking. In this study, we perform computer modeling of earthquake sequences that are coupled to the evolution of fluid pressure and rock properties. In particular, compaction or dilation of the water-filled pore space in rock drives changes in fluid pressure and influences the fault's frictional resistance to slip. The model quantifies the effects of compaction and dilation on both large earthquakes and slow slip events,

Corresponding author: Yuyun Yang, yuyunyang@cuhk.edu.hk

42 providing specific predictions regarding slow slip event properties, pressure changes, and
 43 changes in fluid flow that might be testable with geophysical, geologic, and geochemi-
 44 cal data.

45 2 Introduction

46 The role of fluids in controlling fault zone strength and the occurrence of earthquakes,
 47 slow slip events, and aseismic slip has been recognized for many decades. The focus on
 48 fluids has mounted in recent years as new observations are linking fluids to slow slip and
 49 possibly even the nucleation of great earthquakes (Saffer & Bekins, 1998; Ito et al., 2007;
 50 Frank et al., 2015; Khoshmanesh & Shirzaei, 2018; Ruiz & Madariaga, 2018; Warren-
 51 Smith et al., 2019; Gosselin et al., 2020; Sibson, 2020; Pritchard et al., 2020). Fluids are
 52 present throughout the seismogenic zone and below it, with much evidence for pore fluid
 53 pressures in excess of hydrostatic at depth. Fluid flow and pore pressure are also likely
 54 to be dynamic quantities, varying over coseismic to interseismic timescales, as a conse-
 55 quence of nonlinear coupling between slip and fluid transport properties like porosity and
 56 permeability (Sibson, 1992a).

57 The processes influencing fluid transport and its coupling to slip depend on the tec-
 58 tonic environment and the pressure-temperature conditions associated with different depths.
 59 In the seismogenic zone, fault slip is localized within a low permeability fault core, which
 60 is surrounded by a damage zone having elevated permeability and storage capacity (Caine
 61 et al., 1996; Faulkner et al., 2010). Fluids are preferentially channeled along faults, with
 62 along-fault transport occurring primarily within the damage zone. Cataclastic fault rocks
 63 are formed by fracturing and rotation of mineral grains and grain fragments accompa-
 64 nied by dilatancy and frictional sliding along grain boundaries (Woodcock & Mort, 2008).
 65 Low strain rate deformation can also occur through fluid-assisted diffusive mass trans-
 66 fer and pressure solution (Rutter, 1983; Renard et al., 2000; Fagereng & Toy, 2011; Gratier
 67 et al., 2013). Near the base of the seismogenic zone, which is the primary focus of our
 68 study, elevated temperatures activate other deformation mechanisms and chemical pro-
 69 cesses that influence fluid transport and pore pressure dynamics. We separate our dis-
 70 cussion here by tectonic environment, briefly reviewing faults in both continental crust
 71 and subduction zones.

72 In the continental crust, deviatoric stresses decrease in the lower crust due to the
 73 onset of dislocation creep (Byerlee, 1978; Goetze & Evans, 1979; Brace & Kohlstedt, 1980;
 74 Poirier, 1985; Karato, 2008), sometimes also accompanied by fluid-assisted diffusive mass
 75 transfer and pressure solution (Rutter, 1983; Renard et al., 2000; Gratier et al., 2003;
 76 Fagereng & Toy, 2011; Gratier et al., 2013). Deformation is distributed across a broader
 77 shear zone (Molnar et al., 1999; Norris & Cooper, 2003; Fossen & Cavalcante, 2017), though
 78 there is also much evidence for a transitional region exhibiting both localized frictional
 79 shear and distributed deformation (Cole et al., 2007; Frost et al., 2011; Kirkpatrick &
 80 Rowe, 2013). Fluids are channeled upward along faults, with fluid sources including me-
 81 teoric water, mantle-derived fluid, and fluids released during metamorphic dehydration
 82 reactions (Kennedy et al., 1997; Faulkner & Rutter, 2001; Fulton & Saffer, 2009; Men-
 83 zies et al., 2016). In certain locations, such as the central section of the San Andreas Fault,
 84 fluids are also sourced by dehydration reactions within paleo-subduction rocks (Bürgmann,
 85 2018). Tremor and slow earthquakes occur in the lower crust below the seismogenic zone,
 86 at depths of ~15-30 km, on the San Andreas Fault near Parkfield (Shelly & Hardebeck,
 87 2010; Rousset et al., 2019). Correlations between tremor and tidal forcing provide ev-
 88 idence for low effective normal stress and near-lithostatic pore fluid pressures.

89 Fluids are arguably even more important in subduction zones. In the shallow ac-
 90 cretionary prism, mechanical compaction of subducting sediments creates overpressure
 91 (Saffer & Tobin, 2011), which many have linked to shallow slow slip events (Saffer & Wal-
 92 lace, 2015; Araki et al., 2017; Bürgmann, 2018). At greater depths, near and below the

base of the seismogenic zone, increasing temperatures and pressures activate various dehydration reactions (Hyndman & Peacock, 2003; Hacker et al., 2003; Peacock, 2009; Fagereng & Diener, 2011; Condit et al., 2020). Fluids can also be sourced by volatile release from the mantle (Kerrick & Connolly, 2001). Slow slip and tremor at these depths are widespread across many subduction zones (Schwartz & Rokosky, 2007; Beroza & Ide, 2011; Bürgmann, 2018) and fluid pressures are again thought to be close to lithostatic (Schwartz & Rokosky, 2007; Audet et al., 2009; Peacock et al., 2011; Saffer & Wallace, 2015; Condit & French, 2022). Fault structure and deformation is complex as a consequence of the compositional, and hence rheological, heterogeneity and layering within the subducting oceanic crust and overriding plate (Behr & Bürgmann, 2021; Kirkpatrick et al., 2021).

The goal of our work is to quantitatively explore controls on fault zone fluid transport, pore pressure evolution, and their coupling to fault slip using the modern framework of earthquake sequence modeling. While this is done in the context of a vertical strike-slip fault model, described subsequently, we anticipate that many of the general findings are applicable also to subduction zones. We are primarily concerned with the longer timescales relevant to slow earthquakes and earthquake cycle dynamics, for which along-fault fluid flow and pressure diffusion in fault damage zones are important. We assume pressure equilibration across the width of the fault zone, such that the pressure on slip surfaces within the fault core is approximately the same as the pressure within the damage zone. This is valid at timescales exceeding the hydraulic diffusion time across the fault zone width. For example, the diffusion time across 20 m is approximately 1 day for a hydraulic diffusivity of 10^{-3} m²/s. Fault cores can have much lower diffusivity $\sim 10^{-6}$ m²/s (Wibberley, 2002) and fault-normal pressure diffusion, over diffusion lengths $\sim 10^{-3}$ m, must be considered for shorter timescale processes such as thermal pressurization (Rice, 2006). We do not consider these processes and thus emphasize that the relevant fluid transport properties at longer timescales are those of the damage zone. We also assume that fluid sources are deeper than our region of interest, and that fluids are channeled upward along the fault zone, so the only relevant processes are those controlling porosity and permeability and hence fluid ascent.

The processes that we will study include changes in porosity from dilatancy and compaction. Porosity is one of the key controls on permeability, with permeability commonly assumed to have a power-law relation to porosity (Mavko et al., 2020). Dilatancy refers to inelastic opening of pore space through fracture and shearing, which if occurring under undrained conditions, creates a suction (reduction in pore pressure) that can stabilize against frictional slip and shearing. Compaction is the opposite, inelastic closure of pore space, and can occur through granular flow, closure of microcracks and fissures, and also as creep closure of pores from viscous flow of the matrix and chemical dissolution-precipitation processes. Changes in porosity can also be elastic, referring to reversible porosity changes caused by changes in effective normal stress. Dilatancy and compaction have been observed in many experiments involving shearing of fluid-saturated gouge and sliding of rough surfaces (Marone et al., 1990; Faulkner et al., 2018; Proctor et al., 2020; Brantut, 2020). Segall and Rice (1995) introduced a widely used model for dilatancy (and compaction) that has received much attention as a possible stabilizing mechanism to help explain slow earthquakes (Segall et al., 2010; Liu & Rubin, 2010; Segall & Bradley, 2012). Others have used similar models (Suzuki & Yamashita, 2009). The Segall and Rice (1995) model is inspired by models used in critical state soil mechanics (Wood, 1990) and is arguably most applicable to shearing of fault gouge. It is not obvious whether it is an appropriate model for dilatancy occurring within the damage zone and broader fault zone. Coseismic dilatancy in the damage zone during rupture propagation is likely controlled by the inelastic yielding that occurs during the passage of the stress concentration at the rupture front (Andrews, 2005; Templeton & Rice, 2008; Viesca et al., 2008). Slow earthquakes also feature stress concentrations at slip fronts so could conceivably activate dilatancy in a similar manner. The abundance of veins in exhumed rocks from the base of the seismogenic zone and at the depths of slow earthquakes

147 (Hickman et al., 1995; Behr & Bürgmann, 2021; Kirkpatrick et al., 2021) demonstrates
148 that dilatancy is important at these greater depths, as well.

149 In addition to the compaction that is described by the Segall and Rice (1995) model,
150 we also account for compaction by creep closure of pores by viscous flow of the matrix
151 and/or fluid-mediated mass transfer processes. Viscous matrix flow occurs through the
152 thermally activated deformation mechanisms discussed earlier, such as pressure solution,
153 dislocation creep, and other crystal plastic flow mechanisms, and therefore becomes more
154 important at depth where temperatures are higher. The closure of cracks and pores can
155 also occur through chemical processes like the dissolution and precipitation of silica or
156 other minerals, cementation, and crack healing (Hickman et al., 1995; Renard et al., 2000;
157 Morrow et al., 2001; Gratier et al., 2003; Cox, 2005; Saishu et al., 2017; Williams & Fagereng,
158 2022). Compaction-driven pressurization and weakening of faults, which occurs on in-
159 terseismic or even longer timescales, was proposed several decades ago (Walder & Nur,
160 1984; Nur & Walder, 1992; Sleep & Blanpied, 1992, 1994; Miller et al., 1996; Miller &
161 Nur, 2000). Those authors explored, through early versions of earthquake sequence mod-
162 els, the occurrence of cycles of interseismic pressurization and weakening, coseismic en-
163 hancement of porosity and permeability, and postseismic depressurization from fluid dis-
164 charge. These models captured many features that were observed geologically and ex-
165 plained in terms of fault valving (Sibson, 1992a). More recent studies have also exam-
166 ined creep compaction. Skarbek and Rempel (2016) introduced a fluid transport and pore
167 pressure evolution model with porosity changes from dehydration reactions and creep
168 compaction. Their model produces porosity waves whose periodicity bears similarity to
169 the recurrence interval of slow slip events in subduction zones, though the model does
170 not explicitly account for frictional slip. A similar model that also produces porosity waves
171 was introduced by Yarushina et al. (2020), who performed a detailed study of the response
172 of a fluid-filled pore to plastic and viscoplastic matrix deformation under combined pres-
173 sure and shear loading.

174 Compaction, fault valving, and related topics are receiving renewed attention given
175 recent advances in earthquake sequence modeling and observations of slow earthquakes
176 and other fluid-related faulting phenomena. Petrini et al. (2020), Dal Zilio and Gerya
177 (2022), and Dal Zilio, Hegyi, et al. (2022) utilized a geodynamic modeling approach, re-
178 cently extended to earthquake sequences, to study the influence of fluids and pore pres-
179 sure changes on shear localization, fault formation, and earthquake occurrence. Their
180 models employ a poro-visco-elastic-plastic rheology with slip distributed across a finite
181 width shear zone in which effective shear viscosity is reduced relative to the surround-
182 ing rock to mimic frictional sliding. This is in contrast to most other earthquake sequence
183 models that idealize faults as frictional interfaces. Their models feature coseismic, rather
184 than interseismic, compaction and pressurization. Pressurization-driven weakening, rather
185 than frictional weakening, is the primary control on earthquake stress drop and rupture
186 propagation. We return to these studies in the Discussion section, after having presented
187 our model and results, to explain why their model and its predictions differ from ours
188 and others in the literature.

189 Another earthquake sequence model accounting for fluid flow and pore pressure dy-
190 namics was introduced by Zhu et al. (2020) to study fault valving. Zhu et al. (2020) in-
191 troduced an evolution equation for permeability, rather than porosity, with permeabil-
192 ity increasing with slip and decreasing with time, the latter as a proxy for healing and
193 sealing processes. The model produced fluid-driven aseismic slip events at the base of
194 the seismogenic zone as well as swarm-like seismicity in the seismogenic zone, both oc-
195 ccurring in concert with the ascent of a fluid overpressure pulse. Permeability changes of
196 several orders of magnitude led to intermittent fluid flow, characteristic of fault valving.
197 This model lacks dilatancy and the stabilizing effects of dilatant suctions, as a consequence
198 of evolving permeability directly with porosity held fixed. It can be viewed as an end-
199 member model accounting only for changes in permeability in response to changes in tor-

tuosity or pore connectivity, rather than porosity itself. Our present study explores the opposite end-member model, in which permeability evolves only in response to changes in porosity. As we demonstrate below, this model does not produce fault valving, at least for the chosen parameters, but nonetheless generates pore pressure dynamics that have a fundamental influence on fault slip. Our model produces aseismic slip events akin to slow earthquakes, in fact with many similar features to the slow earthquakes in Zhu et al. (2020), but caused by a different mechanism. As the present time, it is unclear which model, if either, provides a better description of reality, and we provide suggestions in the Discussion section on experimental and geological studies that might help discriminate between these two end-member models.

3 Model

3.1 Elasticity and Friction

We utilize a model setup (Figure 1) similar to Allison and Dunham (2018) and Zhu et al. (2020) by considering the 2D antiplane shear problem of a planar, vertical strike-slip fault embedded in a linear elastic medium. The fault is located at $y = 0$, z measures depth with respect to the free surface at $z = 0$, and displacements $u(y, z, t)$ are in the x -direction. We exploit symmetry conditions about $y = 0$ and solve the elasticity problem only for one side of the fault ($y > 0$).

The governing equations for antiplane shear deformation are

$$\rho \frac{\partial^2 u}{\partial t^2} = \frac{\partial \sigma_{xy}}{\partial y} + \frac{\partial \sigma_{xz}}{\partial z}, \quad \sigma_{xy} = \mu \frac{\partial u}{\partial y}, \quad \sigma_{xz} = \mu \frac{\partial u}{\partial z}, \quad (1)$$

where σ_{xy} and σ_{xz} are the stress changes associated with displacement u , and ρ and μ are the density and shear modulus, which we assume are constant. Symmetry conditions allow us to define slip and slip velocity as

$$\delta(z, t) = 2u(0, z, t) \quad \text{and} \quad V(z, t) = \partial \delta / \partial t, \quad (2)$$

respectively. The fault boundary conditions are

$$\tau = f(\theta, V)\sigma', \quad (3)$$

$$\dot{\theta} = G(\theta, V), \quad (4)$$

where $\tau(z, t)$ is the shear stress, $\sigma'(z, t) = \sigma'_0(z) - p(z, t)$ is the effective normal stress where σ'_0 is the effective normal stress on the fault with hydrostatic pressure and p is the overpressure (the difference between pore pressure and hydrostatic pressure, $p_{\text{hydro}} = \rho_f g z$, where ρ_f is the fluid density and g is gravity). Equation (3) sets the shear stress equal to the frictional strength, where $f(\theta, V)$ is the rate-and-state friction coefficient and $\theta(z, t)$ is the state variable. Equation (4) is the state evolution equation.

We switch between the quasi-dynamic approximation with radiation damping (Rice, 1993) at low slip velocities (for which the radiation-damping term is effectively negligible) and a dynamic solver with full inertial effects at high slip velocities (Duru et al., 2019). In the quasi-dynamic approximation,

$$\tau(z, t) = \tau_0 + \sigma_{xy}(0, z, t) - \eta_{\text{rad}} V, \quad (5)$$

where τ_0 is the initial shear stress and $\eta_{\text{rad}} = \rho c / 2$ is the radiation damping parameter with $c = \sqrt{\mu / \rho}$ being the S-wave speed. In the dynamic solver, we disable radiation damping. Switching between quasi-dynamic and fully dynamic solvers is based on the nondimensional ratio $R = \eta_{\text{rad}} V / \tau_{qs}$, where the numerator is the radiation damping term and the denominator is the quasi-static shear stress (Duru et al., 2019). We choose $R = 2 \times 10^{-4}$ to control switching into and out of the fully dynamic solver.

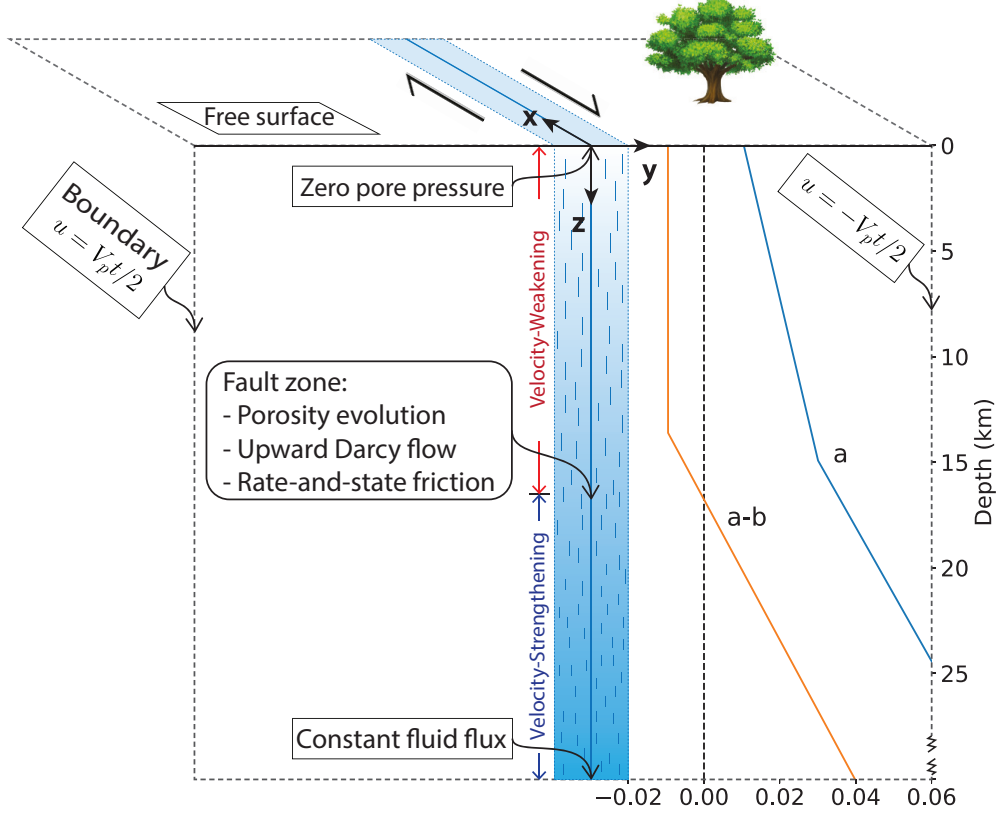


Figure 1. Strike-slip earthquake sequence simulations in a linear elastic solid with rate-and-state friction, fault zone fluid transport, and pore pressure evolution; distributions of rate-and-state parameters a and $a - b$ are shown on the right. Modified from Zhu et al. (2020).

For the computation of the rate-and-state friction coefficient, we use the regularized form (Rice et al., 2001):

$$f(\theta, V) = a \sinh^{-1} \left(\frac{V}{2V^*} e^{f^*/a} \left(\frac{V^* \theta}{d_c} \right)^{b/a} \right), \quad (6)$$

where a is the direct effect parameter and V^* is the reference velocity. We use the aging law for state evolution (Ruina, 1983; Marone, 1998):

$$G(\theta, V) = \frac{bV^*}{d_c} \left(\frac{d_c}{V^* \theta} - \frac{V}{V^*} \right). \quad (7)$$

Apart from the fault boundary condition, the computational domain during the quasi-dynamic phase has three other boundary conditions:

$$\sigma_{xz}(y, 0, t) = 0, \quad \sigma_{xz}(y, L_z, t) = 0, \quad u(L_y, z, t) = \frac{V_L t}{2}, \quad (8)$$

where L_y and L_z are dimensions of the domain in the y and z directions. The boundaries perpendicular to the fault are traction-free, and the displacement condition on the remote boundary parallel to the fault provides steady loading consistent with slip velocity V_L . During the fully dynamic phase, we continue to enforce the friction law on the

234 fault and free surface condition on the top boundary, but we switch at a nonreflecting
 235 condition on the side and bottom boundaries, consistent with the radiation condition that
 236 permits outgoing waves. We use a sufficiently large simulation domain to ensure that the
 237 solution is relatively insensitive to L_y and L_z , as explored by Erickson et al. (2022).

238 3.2 Porosity, Permeability and Fluid Equations

239 Fluid transport and pore pressure evolution are confined to a fault zone of constant
 240 width. As explained in the Introduction, the relevant transport properties of the fault
 241 zone should be regarded as those of the higher permeability and storage damage zone
 242 surrounding the slip surface.

We describe the evolution of fault zone porosity, ϕ , by additively decomposing it
 into elastic, viscous, and plastic components:

$$\dot{\phi} = \dot{\phi}_{\text{elastic}} + \dot{\phi}_{\text{viscous}} + \dot{\phi}_{\text{plastic}}, \quad (9)$$

243 where the overdot denotes a partial time derivative.

Elastic changes in porosity are governed by (Walder & Nur, 1984; Mavko et al., 2020)

$$\frac{\dot{\phi}_{\text{elastic}}}{\phi} = \beta_\phi \frac{\partial p}{\partial t}, \quad (10)$$

where β_ϕ is the elastic pore compressibility. This can be integrated, with fixed total stress,
 to obtain

$$\phi = \phi_0 e^{-\beta_\phi \sigma'}, \quad (11)$$

244 where ϕ_0 is the porosity at zero effective stress. While some experiments are better fit
 245 by adding a residual porosity (Rutqvist et al., 2002), that is, a nonzero value for ϕ in the
 246 large σ' limit, we neglect this complication in our study.

We model the viscous porosity change using a thermally activated linear creep law
 with compaction occurring in response to nonzero effective normal stress (Skarbek & Rem-
 pel, 2016; Yarushina et al., 2020):

$$\frac{\dot{\phi}_{\text{viscous}}}{\phi} = -\sigma' A e^{-E_a/RT} = -\frac{\sigma'}{\eta_s}, \quad (12)$$

247 where E_a is the activation energy, R is the ideal gas constant, T is the temperature, and
 248 A is a rate factor. We can interpret η_s/ϕ as an effective bulk viscosity of the porous rock
 249 that arises from deviatoric viscous strain in the matrix surrounding the pores, in which
 250 interpretation η_s is approximately the shear viscosity of the matrix. Similar equations
 251 describe compaction driven by pressure solution-deposition processes (Walder & Nur,
 252 1984; Renard et al., 2000; Gratier et al., 2013). In either case, there is a strong depen-
 253 dence on temperature that appears here in a standard Arrhenius term. The interpreta-
 254 tion of η_s as the matrix shear viscosity is most valid for equidimensional (spherical or
 255 ellipsoidal) pores, whereas for crack-like pores, the effective bulk viscosity is compara-
 256 ble to the matrix shear viscosity with minimal dependence on porosity (Sleep & Blan-
 257 pied, 1992, 1994). Equation (12) shows that compaction occurs over time scale $t_c = \eta_s/\sigma'$.

In the absence of a porosity production mechanism, viscous creep closure of pores
 would occur until either all fluids are expelled from the pores or, in an undrained case,
 pressure equilibrates with the confining stress. There is no steady state solution with nonzero
 effective normal stress in this case, which is unreasonable for an active fault. Therefore
 we must account for slip-induced fracturing and other inelastic deformation processes
 that increase porosity. The specific processes in the seismogenic zone include cracking
 and fracturing in the fault damage zone during the passage of the stress concentration
 at the rupture front (McGrath & Davison, 1995; Kim et al., 2004) as well as dilatancy

during sliding and shear of geometrically complex surfaces and structures (Lockner & Byerlee, 1994; Segall & Rice, 1995; Faulkner et al., 2010; Proctor et al., 2020; Brantut, 2020). Below the seismogenic zone, the processes that maintain porosity are less well understood, but may also involve brittle deformation and fracturing. Crack-seal shear and extension veins in subduction mélange provide evidence of frictional sliding and tensile fracturing at near-lithostatic fluid pressures (Ujiie et al., 2018; Schmidt & Platt, 2022; Condit & French, 2022), and hydraulic gradients established by local and cyclic pressure variations during viscous creep can drive episodic fluid escape and result in brittle-viscous fault slip (Menegon & Fagereng, 2021; Behr & Bürgmann, 2021). Much work is needed to formulate appropriate mathematical descriptions of these complex processes. Here we utilize an extension of the Segall and Rice (1995) plastic porosity evolution model for dilatancy:

$$\dot{\phi}_{\text{plastic}} = \frac{V}{L}(\phi_{\text{max}} - \phi), \quad (13)$$

where L is the porosity enhancement length scale and

$$\phi_{\text{max}} = \left(\phi_0 + \epsilon \ln \frac{V}{V_0} \right) e^{-\beta_\phi \sigma'} \quad (14)$$

is the steady state porosity. The steady state porosity increases with the logarithm of slip velocity V with a sensitivity quantified by the dilatancy coefficient ϵ . Experiments suggest values of ϵ on the order of 10^{-4} (Marone et al., 1990; Segall & Rice, 1995; Samuelsson et al., 2009). We have added a dependence of ϕ_{max} on the effective normal stress to account for the elastic dependence of porosity on effective stress. Furthermore, ϕ_0 itself is the maximum porosity reachable at zero effective stress at the slip velocity $V = V_0$. The porosity enhancement time scale is $t_e = L/V$.

We have chosen the porosity enhancement length scale as $L = 1$ m, which leads to comparable compaction and dilation time scales in the region below the seismogenic zone, which as we show develops a spatially uniform porosity distribution under steady state conditions. We recognize that in some studies L is chosen to be the same as d_c , the state evolution distance (Segall & Rice, 1995; Liu & Rubin, 2010), based on the assumption that dilatancy occurs within the shearing gouge layer or nonplanar slip surface. In contrast, our model, focusing on longer timescales, is concerned with dilatancy occurring within the much broader damage zone through which along-fault fluid transport occurs. Another conceptual model, which may be relevant below the seismogenic zone, is of a distributed ductile shear zone (Sibson, 1983; Hughes et al., 2020; Cawood & Platt, 2021). In this latter case, the ratio L/w , w being the shear zone width, can be interpreted as the critical strain for porosity evolution. The discussion above suggests that L might best be chosen as a depth-dependent quantity, selected based on the nature of localized or distributed deformation and the width of the shear zone. However, to simplify the model setup, we have chosen L to be independent of depth.

Combining the expressions above, we write the elastic, viscous, and plastic evolution of porosity as

$$\frac{\partial \phi}{\partial t} = \phi \beta_\phi \frac{\partial p}{\partial t} - \frac{\phi \sigma'}{\eta_s} + \frac{V}{L}(\phi_{\text{max}} - \phi). \quad (15)$$

Conservation of fluid mass, together with a linearized fluid equation of state, Darcy's law in a uniform-width fault zone, and the porosity evolution equation, leads to the 1D pressure diffusion equation:

$$\phi \beta \frac{\partial p}{\partial t} = \frac{\partial}{\partial z} \left(\frac{k}{\eta_f} \frac{\partial p}{\partial z} \right) - \dot{\phi}_{\text{viscous}} - \dot{\phi}_{\text{plastic}} \quad (16)$$

$$= \frac{\partial}{\partial z} \left(\frac{k}{\eta_f} \frac{\partial p}{\partial z} \right) + \frac{\phi \sigma'}{\eta_s} - \frac{V}{L}(\phi_{\text{max}} - \phi) \quad (17)$$

where $\beta = \beta_f + \beta_\phi$ is the sum of the fluid and pore compressibility, η_f is the fluid viscosity, and $k = k(\phi)$ is the porosity-dependent permeability. The absence of the $\rho_f g$

term reflects the fact that we have defined p as the overpressure, i.e., pressure in excess of hydrostatic pressure. Viscous and plastic porosity evolution manifest as source terms in the pressure diffusion equation. The fluid flux, expressed as the Darcy velocity, is given by

$$q = \frac{k}{\eta_f} \frac{\partial p}{\partial z}. \quad (18)$$

The absence of a minus sign means that q is positive for upward flow (in the $-z$ direction).

Next we introduce a model for permeability. In this study we assume a power-law relation between porosity and permeability, which has been widely documented experimentally (Walder & Nur, 1984; Nelson, 1994; Zhu et al., 1995; Civan, 2001; Im et al., 2018):

$$\frac{k}{k_0} = \left(\frac{\phi}{\phi_0} \right)^\alpha, \quad (19)$$

where k_0 and ϕ_0 are the reference permeability and porosity and α is an exponent. Although the exponent α can have a wide range of values depending on the rock type and underlying processes which change the pore space, we have chosen $\alpha = 3$ here due to its common usage in the literature (Schulz et al., 2019). Equation (19) is consistent with the experimentally observed dependence of permeability on effective stress, which is commonly expressed as $k = k_0 e^{-\sigma'/\sigma^*}$, where σ^* is a stress sensitivity parameter (Rice, 1992). This expression follows directly from the elastic dependence of porosity on effective stress given by Equation (10) and the porosity-permeability relation (19), which combine to give $k = k_0 e^{-\alpha \beta_\phi \sigma'}$. The stress sensitivity parameter is identified as $\sigma^* = (\alpha \beta_\phi)^{-1}$.

In our model, we keep k_0 constant. However, there is also an option to evolve k_0 to account for the evolution of tortuosity and pore connectivity (Matyka et al., 2008; Ghanbarian et al., 2013). Even when porosity changes are negligible, the permeability could still be enhanced by slip and deformation if the connectivity of the pore space is greatly improved, especially in low porosity rocks. This possibility was explored by Zhu et al. (2020), who accounted only for elastic changes in ϕ and focused on permeability evolution and fault valving from evolution of k_0 rather than ϕ . Here we take the opposite approach and account for changes in k only in response to changes in ϕ with k_0 held fixed.

The pressure diffusion equation (17) requires two boundary conditions. At the free surface, we hold pressure fixed at its hydrostatic value: $p(0, t) = 0$. At the base of the model, we assume a constant fluid source: $q(L_z, t) = q_0$. This relegates fluid sources to depths well below the seismogenic zone. An important extension of our model is to account for fluid sources within the seismogenic zone and beneath it where slow earthquakes occur.

3.3 Numerical Method

We use a high-order SBP-SAT finite difference method for spatial discretization along with adaptive Runge-Kutta time stepping, with error control on slip and the state variable (Erickson & Dunham, 2014; Allison & Dunham, 2018; Duru et al., 2019). Pressure (17) and elastic porosity (10) are solved implicitly using backward Euler (using operator-splitting at the Runge-Kutta stage level), while slip (2), state variable (7), viscous and plastic porosity (12,13) are solved explicitly with the adaptive Runge-Kutta method (Zhu et al., 2020; Yang & Dunham, 2021).

The spatial discretization along the fault is chosen to adequately resolve the nucleation length for the aging law based on Equation (42) in Rubin and Ampuero (2005):

$$L_\infty \approx \frac{1}{\pi} \left(\frac{b}{b-a} \right)^2 L_b, \quad (20)$$

313 where $L_b = \mu D_c / b\sigma'$ (Dieterich, 1992). We use the value of σ' from the initial steady-
 314 state solution for this computation. Then we take the minimum value of L_∞ and resolve
 315 it using 20 grid points for the velocity-weakening part of the fault. We apply grid stretching
 316 starting from the velocity weakening to velocity strengthening transition all the way
 317 down to the bottom of the domain. Grid stretching is also applied in the fault-normal
 318 direction, with dense grids near the fault, and sparser grids away from the fault.

319 4 Steady-State Solution Balancing Viscous Creep Closure and Dilatancy

321 In this section, we develop and examine the steady state solution to the govern-
 322 ing equations. This solution provides insight into the nominal distribution of porosity,
 323 permeability, pressure, and effective normal stress with depth. We also utilize this so-
 324 lution as the initial condition for time-dependent earthquake sequence simulations, wherein
 325 the solution departs rapidly from steady state to produce earthquakes and slow slip. This
 326 demonstrates that the steady state solution is unstable to perturbations. Whether the
 327 instability arises from velocity-weakening friction, fluid coupling, or some combination
 328 thereof should be assessed through linear stability analysis, which is beyond the scope
 329 of this study.

To find the steady state solution, we set $\partial p / \partial t = 0$, $\partial \phi / \partial t = 0$ and $V = V_0$ equal to the plate loading rate. Balancing viscous compaction (12) with dilatancy (13) provides an expression for porosity in terms of effective normal stress:

$$\phi = \frac{\phi_0 e^{-\beta_\phi \sigma'}}{1 + t_e / t_c}. \quad (21)$$

We also have Darcy's law (18), which at steady state (with flux equal to the specified influx q_0) reads

$$\frac{dp}{dz} = \frac{\eta_f q_0}{k}, \quad (22)$$

330 where the porosity-dependent permeability k is evaluated using (21) in (19). Substitut-
 331 ing this expression into (22) and using $\sigma' = \sigma'_0 - p$ yields a first order nonlinear differ-
 332 ential equation for the steady state $p(z)$ that can be integrated downward in z with ini-
 333 tial condition $p(0) = 0$.

334 The set of parameters shown in Table 1 is used in the steady-state calculation and
 335 earthquake sequence simulations. We select a 30 K/km geotherm for consistency with
 336 previous modeling (Allison & Dunham, 2018). The fault total normal stress minus the
 337 hydrostatic pore pressure is assumed to increase linearly as $d\sigma'_0 / dz = 12.2572 \text{ MPa/km}$,
 338 based on Equation (14) in Allison and Dunham (2018). Fluid transport properties ex-
 339 hibit considerable variation and there are limited constraints on properties at the depths
 340 of interest to us. We select an elastic pore compressibility of $\beta_\phi = 10^{-8} \text{ Pa}^{-1}$ based on
 341 studies of the tidal response of water levels in wells near the San Andreas and other faults
 342 (Xue et al., 2013, 2016; Guo et al., 2021). The reference porosity $\phi_0 = 0.1$ and perme-
 343 ability $k_0 = 2 \times 10^{-16} \text{ m}^2$ are selected to provide a steady state permeability profile
 344 comparable to Zhu et al. (2020). A steady fluid source with influx of $q_0 = 10^{-9} \text{ m/s}$
 345 is imposed at the bottom of the fault, which is within the range of fluxes inferred for
 346 continental plate boundary faults (Kennedy et al., 1997; Menzies et al., 2016).

347 The solution we obtain for steady-state overpressure, effective normal stress, poros-
 348 ity, permeability, and the compaction/enhancement times is shown in Figure 2. We com-
 349 pare solutions for three values of the rate factor A : $A = 5 \times 10^{-14} \text{ Pa}^{-1} \text{ s}^{-1}$ (solid line),
 350 which is selected as the reference case, and two comparison cases, $A = 5 \times 10^{-15} \text{ Pa}^{-1}$
 351 s^{-1} (dotted line) and $A = 5 \times 10^{-13} \text{ Pa}^{-1} \text{ s}^{-1}$ (dashed line). Increasing A is similar
 352 to increasing the geothermal gradient or decreasing the activation energy. For the up-
 353 per 2–3 km, the pore pressure is approximately hydrostatic and the effective stress σ'

Symbol	Description	Value
L_z	Domain size in z direction	100 km
L_y	Domain size in y direction	100 km
T_0	Surface temperature	293 K
T	Temperature	30 K/km geotherm
E_a	Pressure solution activation energy	40 kJ mol ⁻¹
R	Ideal gas constant	8.32 J mol ⁻¹ K ⁻¹
A	Flow law prefactor	5 × 10 ⁻¹⁴ Pa ⁻¹ s ⁻¹
η_f	Fluid viscosity	10 ⁻⁴ Pa s
β_f	Fluid compressibility	10 ⁻⁹ Pa ⁻¹
β_ϕ	Elastic pore compressibility	10 ⁻⁸ Pa ⁻¹
ϕ_0	Porosity at zero stress	0.1
ϵ	Dilatancy coefficient	2 × 10 ⁻⁴
L	Porosity enhancement length scale	1 m
k_0	Permeability at ϕ_0	2 × 10 ⁻¹⁶ m ²
α	Exponent for porosity-permeability relation	3
q_0	Fluid injection rate from the bottom	10 ⁻⁹ m/s
V_0	Initial slip velocity	10 ⁻⁹ m/s
V^*	Reference slip velocity	10 ⁻⁶ m/s
f^*	Reference friction coefficient at V^*	0.6
d_c	State evolution distance	2 mm

Table 1. Parameters used for steady-state calculation and earthquake sequence simulations.

increases linearly. The porosity and permeability are also relatively high in this region, but they experience a rapid decrease as σ' increases due to the elastic porosity response to effective normal stress. At about 5–10 km, σ' reaches a peak of about 90, 70, and 50 MPa, respectively, for increasing values of A . At this peak, porosity also reaches a minimum value as it decreases with increasing σ' . The effective stress σ' then starts to decrease due to compaction. The effect can be seen from Figure 2(d), which shows the time scales for compaction in red and dilatancy in blue. For higher values of A , the point at which dilatancy and compaction exactly balance each other is shallower and the compaction time is shorter. In all, the larger the value of A , the faster compaction happens especially at shallower depths, which results in higher overpressure, lower effective normal stress, and lower porosity and permeability.

Porosity and permeability approach constant values at sufficiently great depths. This asymptotic behavior as $z \rightarrow \infty$ can be understood as follows. We substitute (19) and (21) into (22), and then approximate $e^{-\beta_\phi \sigma'} \approx 1$ because effective stress is very low at depth, to obtain

$$\frac{dp}{dz} \approx \frac{\eta_f q_0}{k_0} \left(1 + \frac{t_e}{t_c}\right)^3. \quad (23)$$

Next, we make the ansatz, to be verified below, that σ' approaches a constant value as $z \rightarrow \infty$ such that $d\sigma'/dz = d\sigma'_0/dz - dp/dz \rightarrow 0$. This allows us to replace dp/dz with the constant $d\sigma'_0/dz$ in (23), which we solve for the asymptotic behavior of the porosity enhancement to compaction time scale ratio:

$$\frac{t_e}{t_c} \approx \left(\frac{d\sigma'_0}{dz} \frac{k_0}{\eta_f q_0} \right)^{1/3} - 1. \quad (24)$$

Substituting parameter values into this expression, we obtain $t_e/t_c \approx 1.91$. Because $t_e = L/V_0 = 31.69$ yr is constant, this means $t_c = (Ae^{-E_a/RT} \sigma')^{-1} \approx t_e/1.91 =$

16.63 yr is also a constant, regardless of the compaction rate factor A . This explains why the compaction time approaches the same value at depth for all A in Figure 2. It also follows that porosity and permeability approach constant values, independent of A , specifically $\phi \approx \phi_0/(1+t_e/t_c) = 0.034$ and $k \approx k_0/(1+t_e/t_c)^3 = 8.16 \times 10^{-18} \text{ m}^2$. The limiting value of effective normal stress (which does depend on A) follows from the above expressions:

$$\sigma' \approx \frac{V_0}{LAe^{-E_a/RT}} \left[\left(\frac{d\sigma'_0}{dz} \frac{k_0}{\eta_f q_0} \right)^{1/3} - 1 \right]. \quad (25)$$

The original ansatz of constant σ' as $z \rightarrow \infty$ is justified.

We remark that the steady-state effective stress profile in Figure 2(a) differs from other models in the literature involving upward flow along faults, in particular the Rice (1992) model that includes the elastic dependence of permeability on effective stress. This model was also adopted by Zhu et al. (2020) for their steady state. The Rice (1992) model features pore pressure than transitions from the hydrostatic gradient near the surface to the fault normal stress gradient at depth, such that effective normal stress is constant over much of the seismogenic zone. This distribution of effective stress has been widely used in earthquake sequence modeling, following Rice (1993). Our model produces a similar distribution of effective stress near the surface and in the upper seismogenic zone, with overpressure developing in response to the elastic dependence of permeability on effective stress. However, after reaching a maximum within the seismogenic zone, it decreases toward a much lower value at depth due to the onset of compaction, which was neglected by Rice (1992).

5 Earthquake Sequence Simulations

Next we turn to earthquake sequence simulations. We start the simulations from steady-state conditions. The hydraulic steady state is described in the previous section. In addition, slip velocity is set to V_0 and state and friction coefficient to their steady state values. However, the steady state solution is unstable, and complex sequences of earthquakes and aseismic slip quickly emerge. We run our simulation for five earthquake cycles to spin up the system.

5.1 Reference Case

In this section, we examine the reference case with $A = 5 \times 10^{-14} \text{ Pa}^{-1} \text{ s}^{-1}$. Figure 3(a) shows the space-time plot of slip velocity. We observe ruptures of the full seismogenic zone happening every 20–30 years, and between those large ruptures, there are about 2 partial ruptures at the base of the seismogenic zone. Leading up to each full or partial rupture is a set of SSEs that happen below the ascending locking depth, which advances about 4–5 km over the cycle. Figure 3(b) is a space-time plot of the effective normal stress over the same time period. Note that the effective stress departs from the steady state prediction, increasing during each earthquake as pore pressure decreases from dilatancy. In Figure 4, we zoom into an 8-year period from about 50–58 years into the simulation (shown as a black box in Figure 3) to study the slow slip pattern in greater detail. In this region, where SSEs occur, the effective stress is between 30–40 MPa, much higher than in other models for slow slip. We return to this point in the Discussion.

Figure 4 shows spontaneously generated SSEs which occur about every year at the base of the seismogenic zone over a period of ~ 8 years, gradually unlocking the fault and pushing the creep front upward before an earthquake occurs. Above the locking depth, the fault is below steady state (except during earthquakes), whereas below it, it is close to steady state, on average. We speculate that SSEs occur here because that steady state is unstable due to velocity weakening friction and compaction-driven pressurization. These SSEs have a wide range of behaviors. Some can last from a few months to a year, which

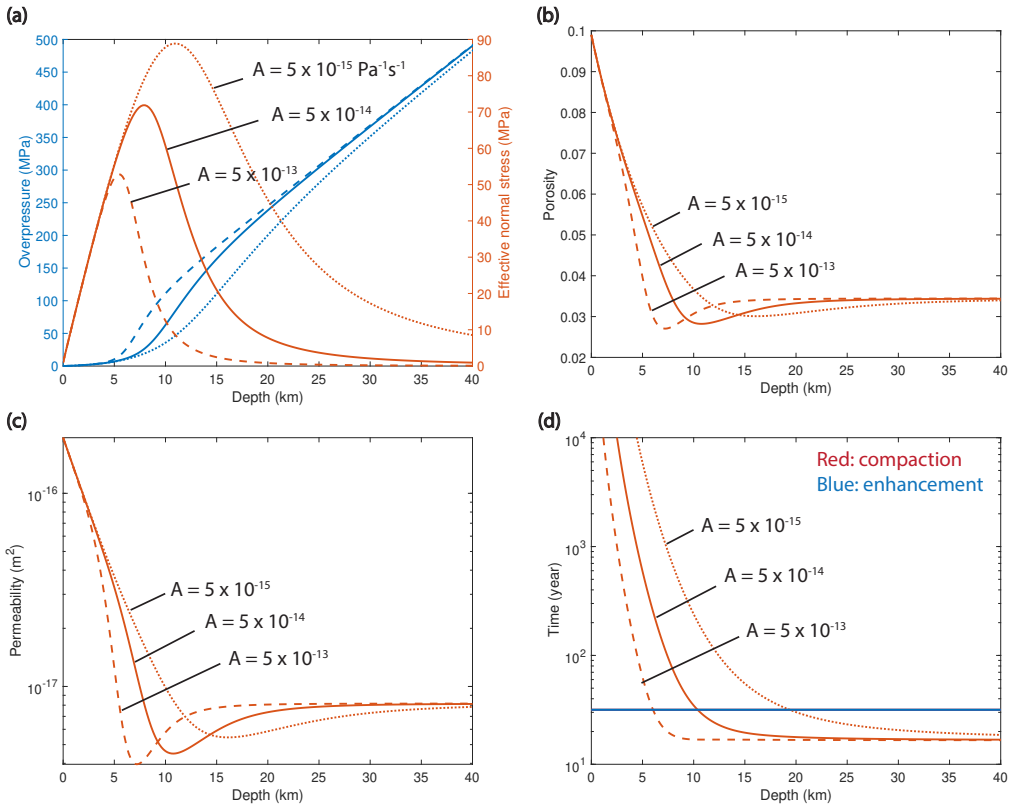


Figure 2. Steady-state solution for different values of compaction rate factor: $A = 5 \times 10^{-15} \text{ Pa}^{-1} \text{ s}^{-1}$ (dotted line), $A = 5 \times 10^{-14} \text{ Pa}^{-1} \text{ s}^{-1}$ (solid line), and $A = 5 \times 10^{-13} \text{ Pa}^{-1} \text{ s}^{-1}$ (dashed line). (a) Overpressure (blue) and effective normal stress (red), (b) porosity, (c) permeability, (d) porosity compaction time t_c (red) and enhancement time t_e (blue). The solution is shown to 40 km depth, but the steady state solution is solved for the entire 100 km domain.

are characteristic of long-term SSEs observed at some subduction zones, such as in southwest Japan in the Nankai subduction zone (Hirose & Obara, 2005; Matsuzawa et al., 2010; Kobayashi, 2017) and in New Zealand (Wallace et al., 2012; Wallace, 2020). There are also shorter-term, high-velocity SSEs that only last for a few days, marked by the deeper red colors that indicate their high velocity in Figure 4(b). We will zoom into these events in more detail later.

Overall, the SSEs are located between about 10–14 km depth, where the fault is entirely velocity weakening. The reason why SSEs nucleate in this region but not further down-dip can be seen in Figure 4(f), which shows the depth dependence of nucleation length. We calculate the nucleation length according to Equation (20) using σ' at the beginning of this period. It is likely that dilatancy, compaction, and fluid coupling alter the nucleation process and nucleation length, but we currently lack an alternative expression for nucleation length that accounts for these processes. Between 10–14 km, the nucleation length ranges from about 100 to 300 m, but below 14 km it grows rapidly to more than 1000 m. Complex SSE patterns occur in the region with short nucleation lengths, but where the nucleation length is larger we do not observe any instabilities.

The SSEs arise because of the velocity weakening friction instability, accelerated in timing by compaction-induced pressurization, but with the increase in slip velocity stalled by dilatancy. The pressure and porosity change relative to the beginning of the

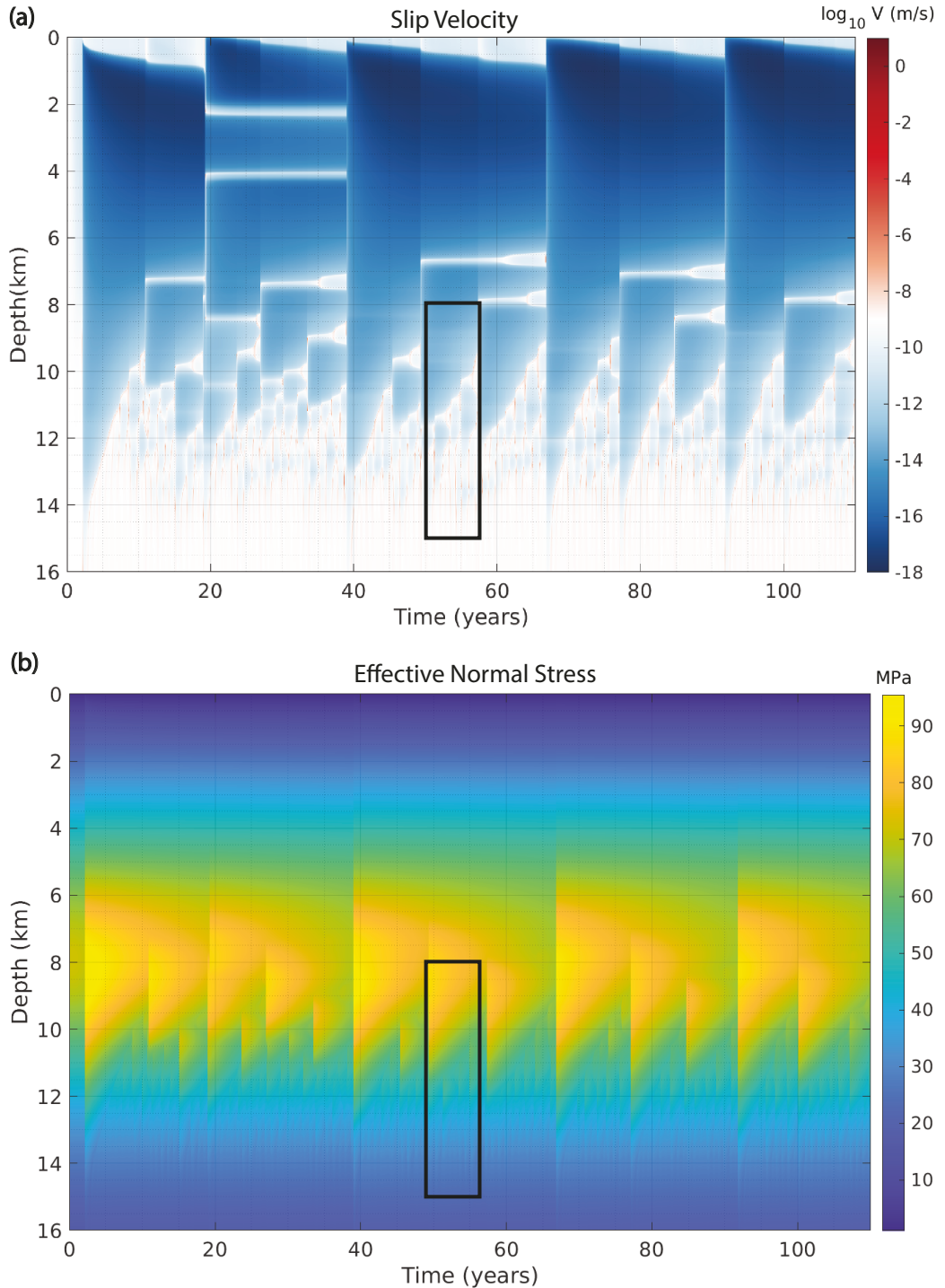


Figure 3. Space-time plot of (a) slip velocity and (b) effective normal stress over 110 years of simulation time. The entire region shown is velocity weakening.

425 selected time period are shown in Figure 4(c) and (d). Before each SSE occurs, compaction-
 426 driven pressurization weakens the fault and causes it to slip. When slip happens, dilatancy opens pore space, reduces pressure and strengthens the fault, limiting slip veloc-
 427

428 ity. The occurrence of slip reduces shear stress and slip velocity eventually decelerates.
 429 Compaction again dominates dilatancy and causes the pressure to rise, and in this fashion
 430 the chain of SSEs is generated. Each successive SSE is able to propagate further into
 431 the shallower section of the fault due to elastic stress transfer during the unlocking pro-
 432 cess. Moreover, pressurization of the fault above the locking depth, which is creeping at
 433 velocities below the plate rate, is driven by pore compaction. Consider the fault at 9.5
 434 km depth, which at the end of the SSEs has experienced a nearly 20 MPa pore pressure
 435 increase. Dilatancy can be ignored here since the slip velocity in this time window is much
 436 lower than the plate loading rate. The compaction time scale at this depth is $t_c \approx 1200$
 437 years, so that the pressurization rate from compaction is $(t_c \phi \beta)^{-1} \approx 2.5$ MPa/yr. For
 438 a period of about 8 years before the earthquake occurs, the pressure increase is approx-
 439 imately 20 MPa. Finally, when a stress concentration has been built up in the lower seis-
 440 mogenic zone where the fault is sufficiently weakened by pressurization, an earthquake
 441 nucleates, resets the shear stress level, and the cycle continues in another episode.

442 We also note that due to the small porosity changes as shown in Figure 4(d), the
 443 permeability changes accompanying these SSEs are also very minor. This means that
 444 changes in fluid flux, shown in Figure 4(e), are concentrated immediately behind advanc-
 445 ing slip fronts where pressure gradients are largest as a consequence of dilatant suctions.
 446 Fluids flow from the undilated region ahead of the slip front into the dilated region be-
 447 hind it, and this flow can be either upward (for a slip front advancing downward) or down-
 448 ward (for a slip front advancing upward). Elevated fluxes and reversals in flow direction
 449 are confined to regions extending no more than a few hundred meters and persist only
 450 for days to months, after which flow returns to its steady state value. This stands in con-
 451 trast to the SSEs that are driven by fault valving and upward fluid migration as seen
 452 in Zhu et al. (2020), where flow is always upward and flux varies over four orders of mag-
 453 nitude. We return to this comparison in the Discussion.

454 We now take a closer look at the SSE that happens about 2 years into the time win-
 455 dow shown in Figure 4(a). This event is rather characteristic of the complex behavior
 456 of slow slip in the simulation. The zoomed-in view of the slip velocity is shown in Fig-
 457 ure 5(a), which spans 3 years. During this time, we first have a spontaneously generated
 458 slow slip transient starting at around 2.5 years from a depth of approximately 14 km that
 459 propagates upward. When it reaches 13 km depth after about 2–3 months, the slip front
 460 splits into an upward- and a downward-propagating front. The downward front slows
 461 down and stabilizes, whereas the upward front continues unlocking the fault and even-
 462 tually merges with another crack tip, which nucleates at 11.5 km depth about 3 years
 463 into the time window. Moreover, at 3.5 years and 4.3 years, close to 13 km depth, two
 464 more such events nucleate, propagating both up and down. Figure 5(b), which shows the
 465 pressure change, illustrates the interaction between compaction and dilatancy. Dilatancy
 466 creates suctions of a few MPa during each event, while compaction in regions of the fault
 467 below steady state continues to pressurize and weaken the fault.

468 The interaction among slip velocity, porosity, and pressure during the 2–5-year pe-
 469 riod can be more clearly seen in Figure 6, where we plot porosity change, pressure change,
 470 and slip velocity at 11.5 km depth for the same time interval shown in Figure 5 (with
 471 changes in porosity and pressure calculated with respect to those values at time zero in
 472 Figure 4). At first, pressure starts to increase as the pores compact. Slip velocity remains
 473 low until the passage of an SSE between time steps 660–680 (or around 3.2 years) that
 474 increases slip velocity to about 10^{-8} m/s. When slip occurs, dilatancy causes a pressure
 475 drop that strengthens the fault. This strengthening contributes to the arrest of the SSE
 476 and brings the slip velocity down to the loading rate.

477 We can understand the quantitative controls on porosity change, and hence per-
 478 meability, during rapid slip (earthquakes and SSEs) as follows. Rapid slip means that
 479 pressure changes from compaction and fluid flow can be neglected, and we write Equa-

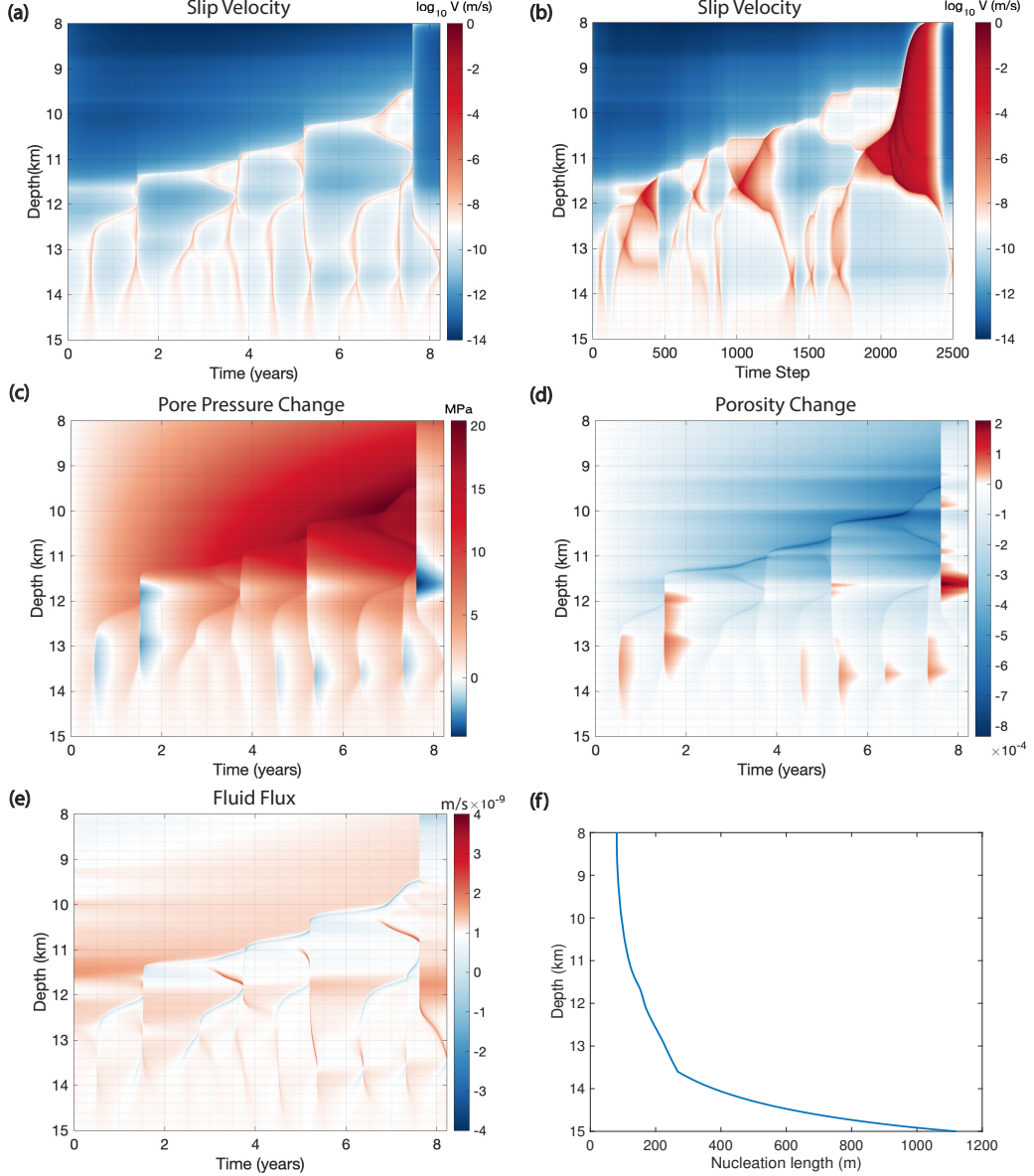


Figure 4. Results from about 50 years into the reference simulation, plotted for depth range 8–15 km over about 8 years, illustrating representative SSE behavior in our simulations. Space-time plots of (a) \log_{10} slip velocity with time on the x-axis, (b) \log_{10} slip velocity with simulation steps on the x-axis, (c) pressure change, (d) porosity change from the beginning of this period, and (e) fluid flux. (f) Nucleation length variation with depth, evaluated using the effective normal stress distribution at the beginning of this period.

tions (15) and (17) as

$$\dot{\phi} \approx \phi \beta \dot{p} + \dot{\phi}_{\text{plastic}}, \quad (26)$$

and

$$\phi \beta \dot{p} \approx -\dot{\phi}_{\text{plastic}}, \quad (27)$$

which combine to yield

$$\dot{\phi} \approx \left(1 - \frac{\beta_\phi}{\beta}\right) \dot{\phi}_{\text{plastic}} = \frac{\beta_f}{\beta_f + \beta_\phi} \dot{\phi}_{\text{plastic}}. \quad (28)$$

Therefore, the larger the pore compressibility β_ϕ is compared to the fluid compressibility β_f (and thus the closer β_ϕ/β is to unity), the smaller the change in total porosity when the fault slips. Note that small changes in porosity do not preclude substantial pressure changes from dilatancy, which are dictated by changes in plastic porosity rather than total porosity. The importance of β_ϕ/β was recognized in a similar manner by Dal Zilio, Hegyi, et al. (2022).

After the first SSE arrests around time step 700, the slip front of the SSE that was generated deeper propagates upward and merges with the SSE that nucleated at 11.5 km. The merging of these slip fronts causes a faster SSE to nucleate at about 11.8 km, which continues to drive the slip front upwards and raise the locking depth. This shows up as the second velocity peak in Figure 6, reaching between 10^{-7} – 10^{-6} m/s. Dilatancy produces a larger pressure drop here than for the previous slower event. After this slip front passes and slip velocity drops below the loading rate, compaction again becomes the dominant process and pressurizes the fault. Although all SSEs could be considered as failed nucleations of an earthquake, some reach higher slip velocities in response to the build-up of spatially average shear stress from deeper slip, or due to stress concentrations left behind by previous ruptures.

The amount of slip at 11.5, 12.5, and 13.5 km depth is plotted in Figure 5(c). At 12.5 and 13.5 km depth, slip accumulates in a more continuous manner, with fastest increases of 1–2 cm of slip during the passage of each slip front that spans a few months. At 11.5 km, a sharp increase in slip between 3.5 and 4 years is attributed to the rapid SSE caused by the merging of an upward- and a downward- propagating slip front. This event creates about 3 cm of slip over only a few days. The shear strength of the fault at the same locations is plotted in Figure 5(d). Strength drops during the passage of the SSEs can exceed 1 MPa but stress drops are generally much smaller. Thus, there is a diversity of slip behavior including both long-term events and high-velocity short-term events. Both can propagate upward and downward, accumulating varying amounts of slip and experiencing different stress and strength drops.

5.2 Comparison with Different Compaction Rate Factors A

In this section, we compare earthquake sequence simulation results for different values of the compaction rate factor A , as examined earlier in the context of the steady state solution (Figure 2). Changing A alters the compaction time scale and hence the depth at which compaction time becomes shorter than the porosity enhancement time scale. As we show, this is the primary control on the depth of SSEs. Observe from the space-time plots of slip velocity in Figure 7 that for the higher value of $A = 5 \times 10^{-13}$ Pa $^{-1}$ s $^{-1}$, the recurrence time interval of large earthquakes has been reduced to less than 10 years, and the location of the SSEs shallows to about 5–9 km depth. This is because higher A causes faster compaction-driven pressurization and weakening. Figure 7(c) shows a zoomed-in view of the boxed region in Figure 7(a). SSEs are spontaneously generated above 9 km depth. The earlier events have a single slip front that propagates upward, but the same type of complexity seen for the reference case emerges for later events at shallow depths of 6–7 km. Here, nucleation drives SSEs both upward and downward, and SSEs merge to nucleate subsequent events with faster slip velocities and shorter durations. A short nucleation length on the order of 100–300 m, as shown in Figure 7 (e), is again responsible for the complex SSEs.

On the other hand, when the compaction rate factor is decreased by an order of magnitude from its reference value to $A = 5 \times 10^{-15}$ Pa $^{-1}$ s $^{-1}$, the recurrence inter-

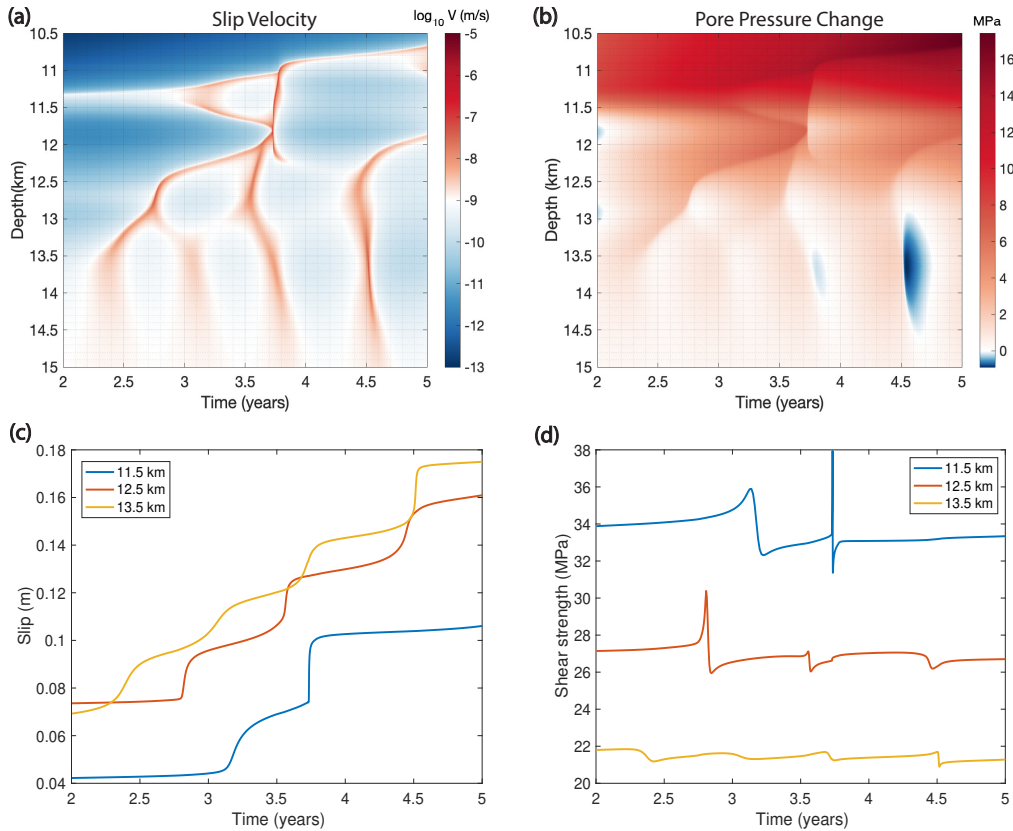


Figure 5. Zoomed-in space-time plot of (a) slip velocity and (b) pressure change (relative to the beginning of the period in Figure 4) of several SSEs. (c) Accumulated slip and (d) fault shear strength at 11.5, 12.5, and 13.5 km depth.

val of large earthquakes increases to about 50 years. The location of SSEs moves deeper to about 14–18 km, where the fault transitions from velocity weakening to velocity strengthening. In Figure 7 (d), we do not see the same complex slip patterns as before, since the region hosting SSEs has longer nucleation lengths due to $a-b$ becoming closer to zero. However, SSEs still spontaneously nucleate below the locking depth and propagate primarily upward, each pushing the locking depth upward by several hundred meters.

For all three compaction rate factors A , SSEs occur in regions where the compaction time becomes comparable to the porosity enhancement time, as shown in Figure 2(d). For $A = 5 \times 10^{-13} \text{ Pa}^{-1} \text{ s}^{-1}$, the two time scales are equal at around 6 km, for $A = 5 \times 10^{-14} \text{ Pa}^{-1} \text{ s}^{-1}$, at 10 km, and for $A = 5 \times 10^{-15} \text{ Pa}^{-1} \text{ s}^{-1}$, at 19 km. For the first two cases, SSEs occur slightly below the depth at which the two time scales are equal, as the fault needs to pressurize and weaken to trigger nucleation of the SSEs, so compaction should dominate over dilatancy at steady sliding conditions. For the last case, SSEs occur above the point of equality, since at 19 km, the fault has already transitioned from velocity weakening to velocity strengthening friction, where it only undergoes stable sliding. This suggests that velocity weakening friction might be a necessary condition for the nucleation and propagation of SSEs in our model. However, the strong influence of the compaction rate factor demonstrates that compaction-driven pressurization and weakening is of fundamental importance for generating SSEs and we cannot rule out the possibility that compaction might permit unstable slip for velocity strengthening friction.

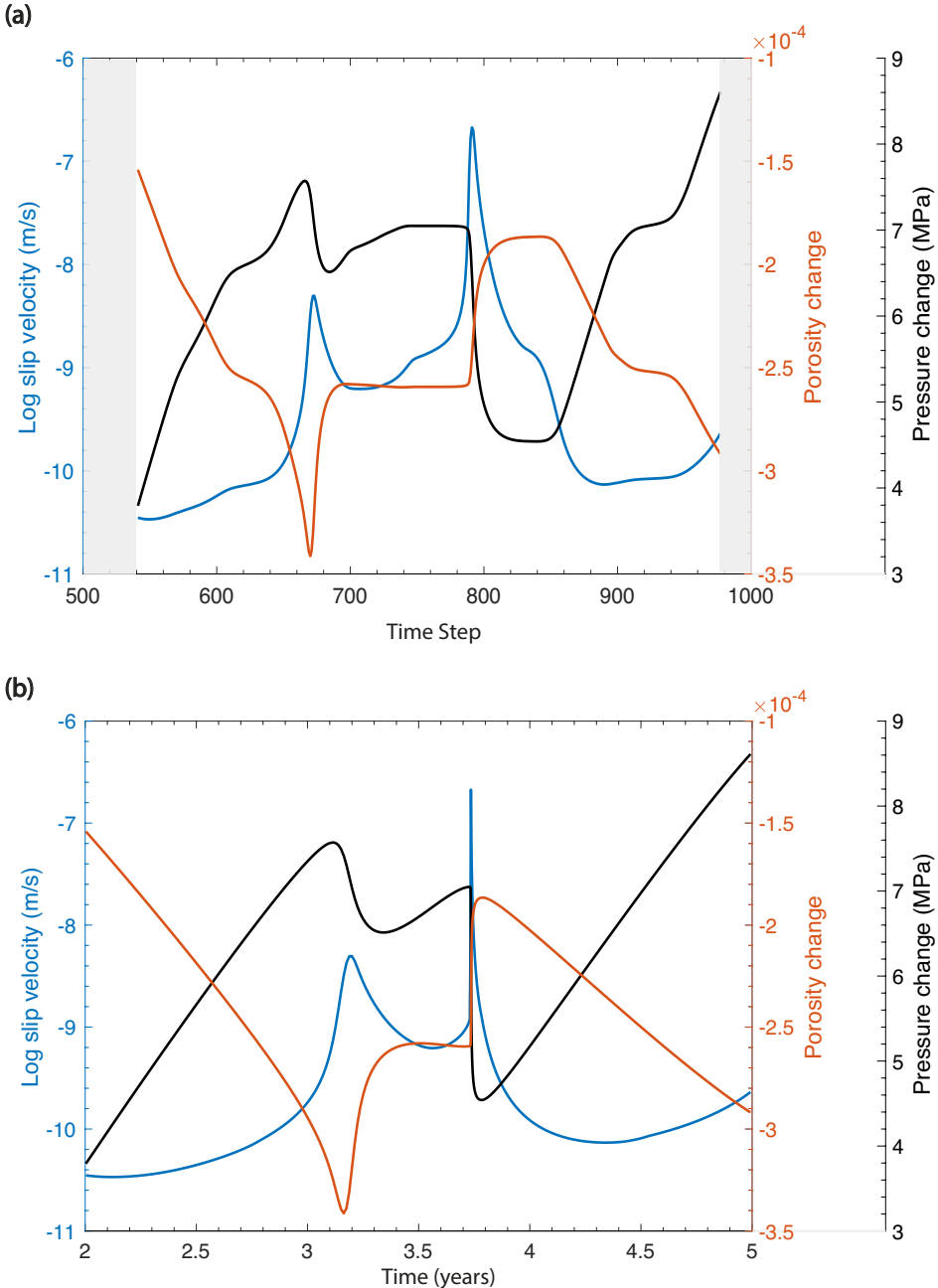


Figure 6. Time series of different fields plotted at 11.5 km depth for the time period in Figure 5: \log_{10} slip velocity (blue), porosity change (red), and pressure change (black) from the beginning of the period in Figure 4. (a) is shown in time steps, (b) is shown in years.

6 Discussion

In this study we have explored the role of thermally activated compaction-driven pressurization in controlling the occurrence of earthquakes and slow slip events. The slip produced by the SSEs in our simulations is on the order of centimeters, spanning a few days to a few years, making them geodetically detectable using GNSS stations and InSAR (Klein et al., 2018; Jolivet & Frank, 2020). The duration and amount of slip of the

545

546

547

548

549

550

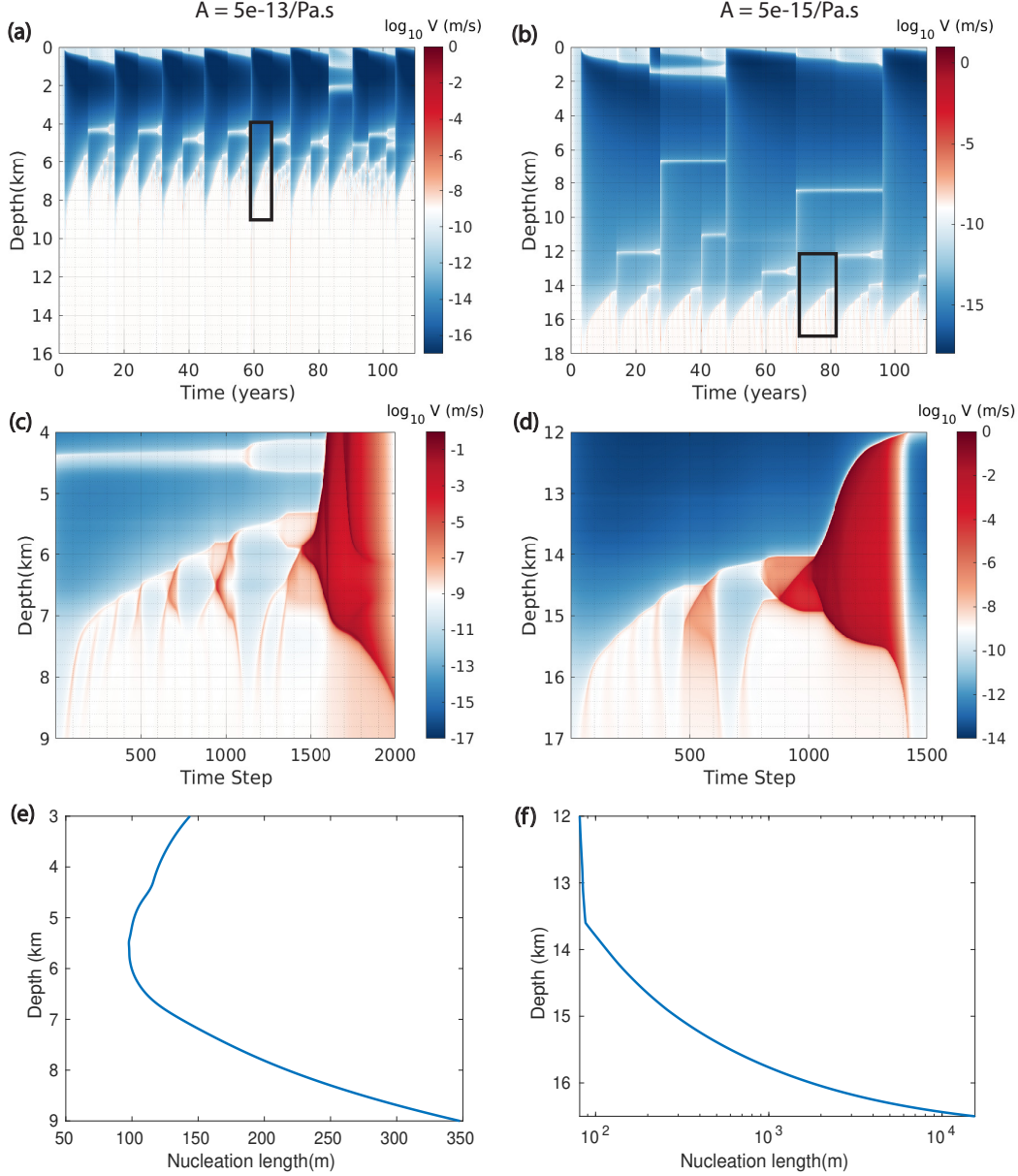


Figure 7. Left column: $A = 5 \times 10^{-13} \text{ Pa}^{-1} \text{ s}^{-1}$. Right column: $A = 5 \times 10^{-15} \text{ Pa}^{-1} \text{ s}^{-1}$. (a), (b): Space-time plots of slip velocity over 110 years. (c), (d): Zoomed-in slip velocity in the region in black box from (a) and (b), note x-axis is time steps of the selected time window. (e), (f) Depth-dependent nucleation length, note in (f), the x-axis is in log scale, since the fault is transitioning from velocity weakening to velocity strengthening starting from about 14 km, $a - b$ becomes closer to zero (velocity neutral) at greater depths, causing the nucleation length to increase by a few orders of magnitude.

SSEs are also in accordance with observations in many subduction zones (Peng & Gomberg, 2010; Radiguet et al., 2011; Araki et al., 2017; Wallace, 2020). However, we note that our model is but one of many models that reproduce geophysically observable constraints on SSEs. This highlights the importance of falsifying models based on geologic and ex-

555 experimental constraints on fault zone structure and the processes controlling pore pres-
 556 sure dynamics and the evolution of fault strength.

557 Our model can be viewed as an end-member case in which permeability is controlled
 558 exclusively by porosity, which evolves in response to creep compaction and dilatancy as
 559 well as elastic pore compressibility. In our simulations, the changes in porosity and there-
 560 fore permeability are quite small. This is because dilatancy-driven porosity increase from
 561 slip is approximately balanced by elastic porosity reduction from the pressure drop. This
 562 balance occurs when the fluid compressibility is much smaller than the pore compress-
 563 ability, such that pore and total compressibilities are approximately equal. Pore compress-
 564 ability is influenced by pore geometry as well as porosity and matrix elastic properties
 565 and there is hence considerable variability and uncertainty. This speaks to the need for
 566 experimental constraints on pore compressibility at relevant pressure and temperature
 567 conditions, as well as geologic constraints on the lithology and pore structure of the rocks
 568 hosting slip.

569 Without large permeability changes, large-scale fluid flux is fairly steady despite
 570 rather large pressure changes (\sim 1 to 10 MPa). Fluid flux does change by an order of mag-
 571 nitude, and can even reverse direction, but these changes are transient and localized to
 572 a few hundred meters behind advancing slip fronts. Our model is therefore rather dif-
 573 ferent from the Zhu et al. (2020) model, in which permeability and hence fluid flux vary
 574 by many orders of magnitude in earthquake cycles that are modulated by fault valving.
 575 Large permeability changes occur because permeability was evolved with porosity held
 576 fixed, which is appropriate when permeability changes are driven by the evolution of tor-
 577 tuosity and pore connectivity rather than through changes in porosity. Slow slip events
 578 occur in both models, but through different mechanisms. In our present study, SSEs are
 579 triggered by weakening from compaction-driven pressurization and velocity-weakening
 580 friction, with slip acceleration stalled by dilatant suctions. In contrast, SSEs in the Zhu
 581 et al. (2020) model are driven by the ascent of fluid overpressure pulses.

582 SSEs in both models occur at the base of the seismogenic zone, below the locking
 583 depth where most models neglecting fluid coupling would predict fairly steady sliding
 584 at the loading rate. However, the combination of fluid coupling and velocity-weakening
 585 friction presumably destabilizes the steady sliding solution, with the slip instabilities tak-
 586 ing the form of SSEs. A testable prediction of the models is that successive SSEs incre-
 587 mentally raise the locking depth, which might be seen geodetically as a gradual unlock-
 588 ing of the seismogenic zone (Mavrommatis et al., 2014; Bruhat & Segall, 2017). Seafloor
 589 geodetic observations are probably required to provide sufficient spatial resolution of these
 590 processes (Bürgmann & Chadwell, 2014).

591 We also note that in our model and the Zhu et al. (2020) model, SSEs occur where
 592 effective normal stress is approximately 20 to 30 MPa. This is higher than in most mod-
 593 els for slow slip, which appeal to effective normal stresses of \sim 0.1–1 MPa. We have not
 594 explored the sensitivity of SSEs in our model to tidal body forces, but note that the ob-
 595 served sensitivity of SSEs and tremor to tides might provide a means to falsify both our
 596 model and the Zhu et al. (2020) model (or at least motivate the exploration of other pa-
 597 rameter choices in those models).

598 An improvement to our model, which would serve to decrease the effective normal
 599 stress, is to account for the reduction in total normal stress acting on the fault in response
 600 to dislocation creep and similar flow mechanisms in the bulk surrounding the fault. That
 601 flow acts to equilibrate all three principal stresses with lithostatic pressure, and then creep
 602 closure of pores would raise pore pressure toward lithostatic. Earthquake sequence mod-
 603 els in viscoelastic solids have been developed (Lambert & Barbot, 2016; Allison & Dun-
 604 ham, 2018; Dal Zilio, Lapusta, et al., 2022; Dal Zilio, Hegyi, et al., 2022), so the next
 605 step is to integrate bulk viscoelasticity with fault zone fluid flow. We note that the model
 606 of Dal Zilio, Hegyi, et al. (2022) and Dal Zilio and Gerya (2022) does this, but with slip

607 on a frictional interface replaced with distributed plastic strain in a finite width shear
 608 zone. To capture frictional weakening, the effective shear viscosity within this shear zone
 609 is reduced by many orders of magnitude. The same shear viscosity is used to set the ef-
 610 fective bulk viscosity that governs creep compaction of pores. This leads to coseismic com-
 611 paction and weakening from pressurization. In contrast, our model utilizes a bulk vis-
 612 cosity that remains relatively constant during earthquakes and SSEs, such that compaction
 613 occurs only over much longer time scales. We argue that this is a more appropriate de-
 614 scription when slip is localized. Clearly more work is required to assess the validity of
 615 these very different models for compaction and its role in earthquake and slip dynam-
 616 ics.

617 Experimental, geochemical, and geologic constraints will also be essential for dis-
 618 tinguishing among models. Both laboratory and field experiments (Guglielmi et al., 2015;
 619 Ishibashi et al., 2018; Im et al., 2019) show evidence for permeability enhancement by
 620 slip, but are generally conducted at pressures and temperatures much lower than those
 621 at the depth of slow earthquakes. Geologic studies provide evidence for cyclic changes
 622 in pore pressure in the form of mineral-filled veins and crack-seal features (Sibson, 1992b,
 623 2000; Cox, 2005, 2010; Sibson, 2017, 2020). Constraints from geochemistry are needed
 624 to ascertain the source of silica and other precipitated minerals that fill the veins, in par-
 625 ticular if those minerals are sourced locally or require transport from greater depths by
 626 ascending fluids (Williams & Fagereng, 2022). Lithium isotope geochemistry appears promis-
 627 ing for resolving the short time scales of earthquake cycles (Penniston-Dorland et al., 2017)
 628 and provides evidence for transient fluid flow events in eclogite-facies subduction rocks
 629 from slow earthquake depths (Hoover et al., 2022). These studies speak to the need for
 630 future modeling efforts to more explicitly account for dissolution, transport, and precip-
 631 itation of silica and other minerals, in addition to fluid flow and pressure dynamics. Given
 632 the strong temperature dependence of reaction kinetics, these models should also account
 633 for shear heating and heat transport by conduction and advection.

634 7 Conclusion

635 We have introduced an earthquake sequence model for a vertical strike-slip fault
 636 in a linear elastic solid with fault zone fluid transport and pore pressure diffusion. We
 637 account for elastic, viscous, and plastic porosity evolution within the fault zone, with per-
 638 meability having a power-law dependence on porosity. The model produces large earth-
 639 quakes in the seismogenic zone, whose recurrence interval is controlled in part by compaction-
 640 driven pressurization and weakening. The model also produces a complex sequence of
 641 slow slip events at the base of the seismogenic zone. The SSEs are driven by the inter-
 642 action between pore compaction which raises fluid pressure and weakens the fault, as well
 643 as pore dilation which decreases fluid pressure and limits the slip instability. The cyclic
 644 behaviors exhibited by the SSEs can range from long-term events lasting from a few months
 645 to years, to very rapid short-term events lasting for only a few days. The accumulated
 646 slip for each event is on the order of centimeters. Our model demonstrates the impor-
 647 tant role that compaction and dilatancy have on fluid pressure and fault slip. While the
 648 modeling is conducted for a vertical strike-slip fault, the processes and behaviors are most
 649 likely relevant across a range of tectonic environments, including subduction zones. Ex-
 650 tends these models to subduction zones, where fluid production rates and fluxes are
 651 generally much higher than for faults in continental crust, is an important next step.

652 8 Open Research

653 The earthquake sequence modeling code, simulation input and output files are avail-
 654 able at <https://doi.org/10.17605/OSF.IO/X7HSW>. Figure 1 is modified from Zhu et
 655 al. (2020) under the Creative Commons license <http://creativecommons.org/licenses/by/4.0/>.

657 **Acknowledgments**

658 This work was funded by the National Science Foundation (EAR-1947448) and US Ge-
 659 ological Survey (G21AP10026). We thank Weiqiang Zhu for assistance with problem set-
 660 up and comments.

661 **References**

662 Allison, K. L., & Dunham, E. M. (2018). Earthquake cycle simulations with rate-
 663 and-state friction and power-law viscoelasticity. *Tectonophysics*, *733*, 232–256.
 664 doi: 10.1016/j.tecto.2017.10.021

665 Andrews, D. (2005). Rupture dynamics with energy loss outside the slip
 666 zone. *Journal of Geophysical Research: Solid Earth*, *110*(B1). doi:
 667 10.1029/2004JB003191

668 Araki, E., Saffer, D. M., Kopf, A. J., Wallace, L. M., Kimura, T., Machida, Y., ...
 669 others (2017). Recurring and triggered slow-slip events near the trench at the
 670 Nankai Trough subduction megathrust. *Science*, *356*(6343), 1157–1160. doi:
 671 10.1126/science.aan3120

672 Audet, P., Bostock, M. G., Christensen, N. I., & Peacock, S. M. (2009). Seismic ev-
 673 idence for overpressured subducted oceanic crust and megathrust fault sealing.
 674 *Nature*, *457*(7225), 76–78. doi: 10.1038/nature07650

675 Behr, W. M., & Bürgmann, R. (2021). What's down there? The structures, materi-
 676 als and environment of deep-seated slow slip and tremor. *Philosophical Trans-
 677 actions of the Royal Society A*, *379*(2193), 20200218. doi: 10.1098/rsta.2020
 678 .0218

679 Beroza, G. C., & Ide, S. (2011). Slow earthquakes and nonvolcanic tremor. *An-
 680 nual review of Earth and planetary sciences*, *39*, 271–296. doi: 10.1146/
 681 annurev-earth-040809-152531

682 Brace, W., & Kohlstedt, D. (1980). Limits on lithospheric stress imposed by lab-
 683 oratory experiments. *Journal of Geophysical Research: Solid Earth*, *85*(B11),
 684 6248–6252. doi: 10.1029/JB085iB11p06248

685 Brantut, N. (2020). Dilatancy-induced fluid pressure drop during dynamic
 686 rupture: Direct experimental evidence and consequences for earthquake
 687 dynamics. *Earth and Planetary Science Letters*, *538*, 116179. doi:
 688 10.1016/j.epsl.2020.116179

689 Bruhat, L., & Segall, P. (2017). Deformation rates in northern Cascadia consist-
 690 ent with slow updip propagation of deep interseismic creep. *Geophysical Jour-
 691 nal International*, *211*(1), 427–449. doi: doi.org/10.1093/gji/ggx317

692 Bürgmann, R. (2018). The geophysics, geology and mechanics of slow fault slip.
 693 *Earth and Planetary Science Letters*, *495*, 112–134. doi: 10.1016/j.epsl.2018.04
 694 .062

695 Bürgmann, R., & Chadwell, D. (2014). Seafloor geodesy. *Annual Review of Earth
 696 and Planetary Sciences*, *42*, 509–534. doi: 10.1146/annurev-earth-060313
 697 -054953

698 Byerlee, J. (1978). Friction of rocks. In *Rock friction and earthquake prediction* (pp.
 699 615–626). doi: 10.1007/BF00876528

700 Caine, J. S., Evans, J. P., & Forster, C. B. (1996). Fault zone architecture and per-
 701 meability structure. *Geology*, *24*(11), 1025–1028. doi: 10.1130/0091-7613(1996)
 702 024<1025:FZAAPS>2.3.CO;2

703 Cawood, T., & Platt, J. (2021). What controls the width of ductile shear zones?
 704 *Tectonophysics*, *816*, 229033. doi: 10.1016/j.tecto.2021.229033

705 Civan, F. (2001). Scale effect on porosity and permeability: Kinetics, model, and
 706 correlation. *AIChE journal*, *47*(2), 271–287. doi: 10.1002/aic.690470206

707 Cole, J., Hacker, B., Ratschbacher, L., Dolan, J., Seward, G., Frost, E., & Frank,
 708 W. (2007). Localized ductile shear below the seismogenic zone: Structural

709 analysis of an exhumed strike-slip fault, Austrian Alps. *Journal of Geophysical*
 710 *Research: Solid Earth*, 112(B12). doi: 10.1029/2007JB004975

711 Condit, C., & French, M. (2022). Geologic evidence of lithostatic pore fluid pressures
 712 at the base of the subduction seismogenic zone. *Geophysical Research Letters*,
 713 49(12), e2022GL098862. doi: 10.1029/2022GL098862

714 Condit, C., Guevara, V., Delph, J., & French, M. (2020). Slab dehydration in warm
 715 subduction zones at depths of episodic slip and tremor. *Earth and Planetary*
 716 *Science Letters*, 552, 116601. doi: 10.1016/j.epsl.2020.116601

717 Cox, S. F. (2005). Coupling between deformation, fluid pressures, and fluid flow in
 718 ore-producing hydrothermal systems at depth in the crust. *Economic Geology;*
 719 *Bulletin of the Society of Economic Geologists*, 100, 39–75.

720 Cox, S. F. (2010). The application of failure mode diagrams for exploring the roles
 721 of fluid pressure and stress states in controlling styles of fracture-controlled
 722 permeability enhancement in faults and shear zones. *Geofluids*, 10(1-2), 217–
 723 233. doi: 10.1111/j.1468-8123.2010.00281.x

724 Dal Zilio, L., & Gerya, T. (2022). Subduction earthquake cycles controlled
 725 by episodic fluid pressure cycling. *Lithos*, 426, 106800. doi: 10.1016/
 726 j.lithos.2022.106800

727 Dal Zilio, L., Hegyi, B., Behr, W., & Gerya, T. (2022). Hydro-mechanical earth-
 728 quake cycles in a poro-visco-elasto-plastic fluid-bearing fault structure.
 729 *Tectonophysics*, 838, 229516. doi: 10.1016/j.tecto.2022.229516

730 Dal Zilio, L., Lapusta, N., Avouac, J.-P., & Gerya, T. (2022). Subduction earth-
 731 quake sequences in a non-linear visco-elasto-plastic megathrust. *Geophysical*
 732 *Journal International*, 229(2), 1098–1121. doi: 10.1093/gji/ggab521

733 Dieterich, J. H. (1992). Earthquake nucleation on faults with rate-and state-
 734 dependent strength. *Tectonophysics*, 211(1-4), 115–134. doi: 10.1016/
 735 0040-1951(92)90055-B

736 Duru, K., Allison, K. L., Rivet, M., & Dunham, E. M. (2019). Dynamic rupture and
 737 earthquake sequence simulations using the wave equation in second-order form.
 738 *Geophysical Journal International*, 219(2), 796–815. doi: 10.1093/gji/ggz319

739 Erickson, B. A., & Dunham, E. M. (2014). An efficient numerical method for
 740 earthquake cycles in heterogeneous media: Alternating subbasin and surface-
 741 rupturing events on faults crossing a sedimentary basin. *Journal of Geophysical*
 742 *Research: Solid Earth*, 119(4), 3290–3316. doi: 10.1002/2013JB010614

743 Erickson, B. A., Jiang, J., Lambert, V., Abdelmeguid, M., Almquist, M., Ampuero,
 744 J. P., ... others (2022). *Incorporating full elastodynamic effects and dip-
 745 ping fault geometries in community code verification exercises for simulations
 746 of earthquake sequences and aseismic slip (SEAS)*. (preprint available at
 747 doi:10.31223/X5NP87)

748 Fagereng, Å., & Diener, J. F. (2011). Non-volcanic tremor and discontinuous
 749 slab dehydration. *Geophysical Research Letters*, 38(15). doi: 10.1029/
 750 2011GL048214

751 Fagereng, Å., & Toy, V. G. (2011). Geology of the earthquake source: an introduc-
 752 tion. *Geological Society, London, Special Publications*, 359(1), 1–16. doi: 10
 753 .1144/SP359.1

754 Faulkner, D., Jackson, C., Lunn, R., Schlische, R., Shipton, Z., Wibberley, C., &
 755 Withjack, M. (2010). A review of recent developments concerning the struc-
 756 ture, mechanics and fluid flow properties of fault zones. *Journal of Structural*
 757 *Geology*, 32(11), 1557–1575. doi: 10.1016/j.jsg.2010.06.009

758 Faulkner, D., & Rutter, E. (2001). Can the maintenance of overpressured fluids in
 759 large strike-slip fault zones explain their apparent weakness? *Geology*, 29(6),
 760 503–506. doi: 10.1130/0091-7613(2001)029<0503:CTMOOF>2.0.CO;2

761 Faulkner, D., Sanchez-Roa, C., Boulton, C., & Den Hartog, S. A. M. (2018). Pore
 762 fluid pressure development in compacting fault gouge in theory, experiments,
 763 and nature. *Journal of Geophysical Research: Solid Earth*, 123(1), 226–241.

764 doi: 10.1002/2017JB015130

765 Fossen, H., & Cavalcante, G. C. G. (2017). Shear zones—a review. *Earth-Science Re-*
766 *views*, 171, 434–455. doi: 10.1016/j.earscirev.2017.05.002

767 Frank, W. B., Shapiro, N. M., Husker, A. L., Kostoglodov, V., Bhat, H. S., &
768 Campillo, M. (2015). Along-fault pore-pressure evolution during a slow-
769 slip event in Guerrero, Mexico. *Earth and Planetary Science Letters*, 413,
770 135–143. doi: 10.1016/j.epsl.2014.12.051

771 Frost, E., Dolan, J., Ratschbacher, L., Hacker, B., & Seward, G. (2011). Direct
772 observation of fault zone structure at the brittle-ductile transition along the
773 Salzach-Ennstal-Mariazell-Puchberg fault system, Austrian Alps. *Journal of*
774 *Geophysical Research: Solid Earth*, 116(B2). doi: 10.1029/2010JB007719

775 Fulton, P. M., & Saffer, D. M. (2009). Potential role of mantle-derived fluids in
776 weakening the San Andreas Fault. *Journal of Geophysical Research: Solid*
777 *Earth*, 114(B7). doi: 10.1029/2008JB006087

778 Ghanbarian, B., Hunt, A. G., Ewing, R. P., & Sahimi, M. (2013). Tortuosity in
779 porous media: a critical review. *Soil science society of America journal*, 77(5),
780 1461–1477. doi: 10.2136/sssaj2012.0435

781 Goetze, C., & Evans, B. (1979). Stress and temperature in the bending lithosphere
782 as constrained by experimental rock mechanics. *Geophysical Journal Interna-*
783 *tional*, 59(3), 463–478. doi: 10.1111/j.1365-246X.1979.tb02567.x

784 Gosselin, J. M., Audet, P., Estève, C., McLellan, M., Mosher, S. G., & Schaeff-
785 fer, A. J. (2020). Seismic evidence for megathrust fault-valve behavior
786 during episodic tremor and slip. *Science advances*, 6(4), eaay5174. doi:
787 10.1126/sciadv.aay5174

788 Gratier, J.-P., Dysthe, D. K., & Renard, F. (2013). The role of pressure solution
789 creep in the ductility of the Earth's upper crust. *Advances in geophysics*, 54,
790 47–179. doi: 10.1016/B978-0-12-380940-7.00002-0

791 Gratier, J.-P., Favreau, P., & Renard, F. (2003). Modeling fluid transfer along
792 California faults when integrating pressure solution crack sealing and com-
793 paction processes. *Journal of Geophysical Research: Solid Earth*, 108(B2). doi:
794 10.1029/2001jb000380

795 Guglielmi, Y., Cappa, F., Avouac, J.-P., Henry, P., & Elsworth, D. (2015). Seis-
796 micity triggered by fluid injection–induced aseismic slip. *Science*, 348(6240),
797 1224–1226. doi: 10.1126/science.aab0476

798 Guo, H., Brodsky, E., Goebel, T., & Cladouhos, T. (2021). Measuring fault zone and
799 host rock hydraulic properties using tidal responses. *Geophysical Research Let-
800 ters*, 48(13), e2021GL093986. doi: 10.1029/2021GL093986

801 Hacker, B. R., Peacock, S. M., Abers, G. A., & Holloway, S. D. (2003). Subduction
802 factory 2. are intermediate-depth earthquakes in subducting slabs linked to
803 metamorphic dehydration reactions? *Journal of Geophysical Research: Solid*
804 *Earth*, 108(B1). doi: 10.1029/2001JB001129

805 Hickman, S., Sibson, R. H., & Bruhn, R. (1995). *Introduction to special section:*
806 *Mechanical involvement of fluids in faulting* (Vol. 100) (No. B7). doi: 10.1029/
807 95JB01121

808 Hirose, H., & Obara, K. (2005). Repeating short-and long-term slow slip events
809 with deep tremor activity around the Bungo channel region, southwest Japan.
810 *Earth, planets and space*, 57(10), 961–972. doi: 10.1186/BF03351875

811 Hoover, W. F., Penniston-Dorland, S., Baumgartner, L., Bouvier, A.-S., Dragovic,
812 B., Locatelli, M., ... Agard, P. (2022). Episodic fluid flow in an eclogite-facies
813 shear zone: Insights from Li isotope zoning in garnet. *Geology*, 50(6), 746–750.
814 doi: 10.1130/G49737.1

815 Hughes, C. A., Jessup, M. J., Shaw, C. A., & Newell, D. L. (2020). Evidence for
816 strain rate variation and an elevated transient geothermal gradient during
817 shear zone evolution in the Cordillera Blanca, Peru. *Tectonophysics*, 794,
818 228610. doi: 10.1016/j.tecto.2020.228610

819 Hyndman, R. D., & Peacock, S. M. (2003). Serpentinization of the forearc mantle. *Earth and Planetary Science Letters*, 212(3-4), 417–432. doi: 10.1016/S0012-821X(03)00263-2

820

821 Im, K., Elsworth, D., & Fang, Y. (2018). The influence of preslip sealing on the permeability evolution of fractures and faults. *Geophysical Research Letters*, 45(1), 166–175.

822

823 Im, K., Elsworth, D., & Wang, C. (2019). Cyclic permeability evolution during re- 824 pose then reactivation of fractures and faults. *Journal of Geophysical Research: Solid Earth*, 124(5), 4492–4506. doi: 10.1029/2019JB017309

825

826 Ishibashi, T., Elsworth, D., Fang, Y., Riviere, J., Madara, B., Asanuma, H., ... 827 Marone, C. (2018). Friction-stability-permeability evolution of a fracture in granite. *Water Resources Research*, 54(12), 9901–9918. doi: 10.1029/2018WR022598

828

829 Ito, Y., Obara, K., Shiomi, K., Sekine, S., & Hirose, H. (2007). Slow earthquakes 830 coincident with episodic tremors and slow slip events. *Science*, 315(5811), 503– 831 506. doi: 10.1126/science.1134454

832

833 Jolivet, R., & Frank, W. (2020). The transient and intermittent nature of slow slip. *AGU Advances*, 1(1), e2019AV000126. doi: 10.1029/2019AV000126

834

835 Karato, S. (2008). Deformation of earth materials. *An Introduction to the Rheology 836 of Solid Earth*, 463.

837

838 Kennedy, B., Kharaka, Y., Evans, W. C., Ellwood, A., DePaolo, D., Thordsen, J., ... 839 Mariner, R. (1997). Mantle fluids in the San Andreas Fault system, California. *Science*, 278(5341), 1278–1281. doi: 10.1126/science.278.5341.1278

840

841 Kerrick, D., & Connolly, J. (2001). Metamorphic devolatilization of subducted ma- 842 rine sediments and the transport of volatiles into the Earth's mantle. *Nature*, 411(6835), 293–296. doi: 10.1038/35077056

843

844 Khoshmanesh, M., & Shirzaei, M. (2018). Episodic creep events on the San An- 845 andreas Fault caused by pore pressure variations. *Nature geoscience*, 11(8), 610– 846 614. doi: 10.1038/s41561-018-0160-2

847

848 Kim, Y.-S., Peacock, D. C., & Sanderson, D. J. (2004). Fault damage zones. *Journal 849 of structural geology*, 26(3), 503–517. doi: 10.1016/j.jsg.2003.08.002

850

851 Kirkpatrick, J. D., Fagereng, Å., & Shelly, D. R. (2021). Geological constraints on 852 the mechanisms of slow earthquakes. *Nature Reviews Earth & Environment*, 2(4), 285–301. doi: 10.1038/s43017-021-00148-w

853

854 Kirkpatrick, J. D., & Rowe, C. D. (2013). Disappearing ink: How pseudotachylytes 855 are lost from the rock record. *Journal of Structural Geology*, 52, 183–198. doi: 10.1016/j.jsg.2013.03.003

856

857 Klein, E., Duputel, Z., Zigone, D., Vigny, C., Boy, J.-P., Doubre, C., & Meneses, 858 G. (2018). Deep transient slow slip detected by survey GPS in the re- 859 gion of Atacama, Chile. *Geophysical research letters*, 45(22), 12–263. doi: 10.1029/2018GL080613

860

861 Kobayashi, A. (2017). Objective detection of long-term slow slip events along the 862 Nankai Trough using GNSS data (1996–2016). *Earth, Planets and Space*, 69(1), 1–12. doi: 10.1186/s40623-017-0755-7

863

864 Lambert, V., & Barbot, S. (2016). Contribution of viscoelastic flow in earthquake 865 cycles within the lithosphere-asthenosphere system. *Geophysical Research Letters*, 43(19), 10–142. doi: 10.1002/2016GL070345

866

867 Liu, Y., & Rubin, A. M. (2010). Role of fault gouge dilatancy on aseismic defor- 868 mation transients. *Journal of Geophysical Research: Solid Earth*, 115(B10414). doi: 10.1029/2010JB007522

869

870 Lockner, D. A., & Byerlee, J. D. (1994). Dilatancy in hydraulically isolated faults 871 and the suppression of instability. *Geophysical Research Letters*, 21(22), 2353– 2356. doi: 10.1029/94GL02366

872

873 Marone, C. (1998). Laboratory-derived friction laws and their application to seismic 874 faulting. *Annual Review of Earth and Planetary Sciences*, 26(1), 643–696. doi:

874 10.1146/annurev.earth.26.1.643

875 Marone, C., Raleigh, C. B., & Scholz, C. (1990). Frictional behavior and constitu-
876 tive modeling of simulated fault gouge. *Journal of Geophysical Research: Solid*
877 *Earth*, 95(B5), 7007–7025. doi: 10.1029/JB095iB05p07007

878 Matsuzawa, T., Hirose, H., Shibasaki, B., & Obara, K. (2010). Modeling short-
879 and long-term slow slip events in the seismic cycles of large subduction
880 earthquakes. *Journal of Geophysical Research: Solid Earth*, 115(B12). doi:
881 10.1029/2010JB007566

882 Matyka, M., Khalili, A., & Koza, Z. (2008). Tortuosity-porosity relation in porous
883 media flow. *Physical Review E*, 78(2), 026306. doi: 10.1103/PhysRevE.78
884 .026306

885 Mavko, G., Mukerji, T., & Dvorkin, J. (2020). *The rock physics handbook*. Cam-
886 bridge university press.

887 Mavromatis, A. P., Segall, P., & Johnson, K. M. (2014). A decadal-scale defor-
888 mation transient prior to the 2011 Mw 9.0 Tohoku-oki earthquake. *Geophysical*
889 *Research Letters*, 41(13), 4486–4494. doi: 10.1002/2014GL060139

890 McGrath, A. G., & Davison, I. (1995). Damage zone geometry around fault tips.
891 *Journal of Structural Geology*, 17(7), 1011–1024. doi: 10.1016/0191-8141(94)
892 00116-H

893 Menegon, L., & Fagereng, Å. (2021). Tectonic pressure gradients during viscous
894 creep drive fluid flow and brittle failure at the base of the seismogenic zone.
895 *Geology*, 49(10), 1255–1259. doi: 10.1130/G49012.1

896 Menzies, C. D., Teagle, D. A., Niedermann, S., Cox, S. C., Craw, D., Zimmer, M.,
897 ... Erzinger, J. (2016). The fluid budget of a continental plate boundary fault:
898 Quantification from the Alpine Fault, New Zealand. *Earth and Planetary*
899 *Science Letters*, 445, 125–135. doi: 10.1016/j.epsl.2016.03.046

900 Miller, S. A., & Nur, A. (2000). Permeability as a toggle switch in fluid-controlled
901 crustal processes. *Earth and Planetary Science Letters*, 183(1-2), 133–146. doi:
902 10.1016/S0012-821X(00)00263-6

903 Miller, S. A., Nur, A., & Olgaard, D. L. (1996). Earthquakes as a coupled shear
904 stress-high pore pressure dynamical system. *Geophysical Research Letters*,
905 23(2), 197–200. doi: 10.1029/95GL03178

906 Molnar, P., Anderson, H. J., Audoine, E., Eberhart-Phillips, D., Gledhill, K. R.,
907 Klosko, E. R., ... others (1999). Continuous deformation versus faulting
908 through the continental lithosphere of New Zealand. *Science*, 286(5439),
909 516–519. doi: 10.1126/science.286.5439.5

910 Morrow, C., Moore, D. E., & Lockner, D. (2001). Permeability reduction in granite
911 under hydrothermal conditions. *Journal of Geophysical Research: Solid Earth*,
912 106(B12), 30551–30560. doi: 10.1029/2000JB000010

913 Nelson, P. H. (1994). Permeability-porosity relationships in sedimentary rocks. *The*
914 *Log Analyst*, 35(03).

915 Norris, R. J., & Cooper, A. F. (2003). Very high strains recorded in mylonites
916 along the Alpine Fault, New Zealand: implications for the deep structure of
917 plate boundary faults. *Journal of Structural Geology*, 25(12), 2141–2157. doi:
918 10.1016/S0191-8141(03)00045-2

919 Nur, A., & Walder, J. (1992). Hydraulic pulses in the Earth's crust. In *International*
920 *geophysics* (Vol. 51, pp. 461–473). doi: 10.1016/S0074-6142(08)62834-X

921 Peacock, S. M. (2009). Thermal and metamorphic environment of subduction
922 zone episodic tremor and slip. *Journal of Geophysical Research: Solid Earth*,
923 114(B8). doi: 10.1029/2008JB005978

924 Peacock, S. M., Christensen, N. I., Bostock, M. G., & Audet, P. (2011). High pore
925 pressures and porosity at 35 km depth in the Cascadia subduction zone. *Geol-*
926 *ogy*, 39(5), 471–474. doi: 10.1130/G31649.1

927 Peng, Z., & Gomberg, J. (2010). An integrated perspective of the continuum be-
928 tween earthquakes and slow-slip phenomena. *Nature geoscience*, 3(9), 599–607.

929 doi: 10.1038/ngeo940

930 Penniston-Dorland, S., Liu, X.-M., & Rudnick, R. L. (2017). Lithium isotope geo-
931 chemistry. *Reviews in Mineralogy and Geochemistry*, 82(1), 165–217. doi: 10
932 .2138/rmg.2017.82.6

933 Petrini, C., Gerya, T., Yarushina, V., van Dinter, Y., Connolly, J., & Madonna, C.
934 (2020). Seismo-hydro-mechanical modelling of the seismic cycle: Methodology
935 and implications for subduction zone seismicity. *Tectonophysics*, 791, 228504.
936 doi: 10.1016/j.tecto.2020.228504

937 Poirier, J.-P. (1985). *Creep of crystals: high-temperature deformation processes in*
938 *metals, ceramics and minerals*. Cambridge University Press. doi: 10.1017/
939 CBO9780511564451

940 Pritchard, M. E., Allen, R. M., Becker, T. W., Behn, M. D., Brodsky, E. E.,
941 Bürgmann, R., ... others (2020). New opportunities to study earth-
942 quake precursors. *Seismological Research Letters*, 91(5), 2444–2447. doi:
943 10.1785/0220200089

944 Proctor, B., Lockner, D. A., Kilgore, B. D., Mitchell, T. M., & Beeler, N. M. (2020).
945 Direct evidence for fluid pressure, dilatancy, and compaction affecting slip
946 in isolated faults. *Geophysical Research Letters*, e2019GL086767. doi:
947 10.1029/2019GL086767

948 Radiguet, M., Cotton, F., Vergnolle, M., Campillo, M., Valette, B., Kostoglodov, V.,
949 & Cotte, N. (2011). Spatial and temporal evolution of a long term slow slip
950 event: the 2006 Guerrero slow slip event. *Geophysical Journal International*,
951 184(2), 816–828. doi: 10.1111/j.1365-246X.2010.04866.x

952 Renard, F., Gratier, J.-P., & Jamtveit, B. (2000). Kinetics of crack-sealing, in-
953 tergranular pressure solution, and compaction around active faults. *Journal of*
954 *Structural Geology*, 22(10), 1395–1407. doi: 10.1016/S0191-8141(00)00064-X

955 Rice, J. R. (1992). Fault stress states, pore pressure distributions, and the weakness
956 of the San Andreas fault. In *International geophysics* (Vol. 51, pp. 475–503).
957 doi: 10.1016/S0074-6142(08)62835-1

958 Rice, J. R. (1993). Spatio-temporal complexity of slip on a fault. *Journal of Geo-
959 physical Research: Solid Earth*, 98(B6), 9885–9907. doi: 10.1029/93JB00191

960 Rice, J. R. (2006). Heating and weakening of faults during earthquake slip. *Journal*
961 *of Geophysical Research: Solid Earth*, 111(B5). doi: 10.1029/2005JB004006

962 Rice, J. R., Lapusta, N., & Ranjith, K. (2001). Rate and state dependent
963 friction and the stability of sliding between elastically deformable solids.
964 *Journal of the Mechanics and Physics of Solids*, 49(9), 1865–1898. doi:
965 10.1016/S0022-5096(01)00042-4

966 Rousset, B., Bürgmann, R., & Campillo, M. (2019). Slow slip events in the roots of
967 the San Andreas Fault. *Science advances*, 5(2), eaav3274. doi: 10.1126/sciadv
968 .aav3274

969 Rubin, A. M., & Ampuero, J.-P. (2005). Earthquake nucleation on (aging) rate and
970 state faults. *Journal of Geophysical Research: Solid Earth*, 110(B11). doi: 10
971 .1029/2005JB003686

972 Ruina, A. (1983). Slip instability and state variable friction laws. *Jour-
973 nal of Geophysical Research: Solid Earth*, 88(B12), 10359–10370. doi:
974 10.1029/JB088iB12p10359

975 Ruiz, S., & Madariaga, R. (2018). Historical and recent large megathrust earth-
976 quakes in Chile. *Tectonophysics*, 733, 37–56. doi: 10.1016/j.tecto.2018.01.015

977 Rutqvist, J., Wu, Y.-S., Tsang, C.-F., & Bodvarsson, G. (2002). A modeling ap-
978 proach for analysis of coupled multiphase fluid flow, heat transfer, and defor-
979 mation in fractured porous rock. *International Journal of Rock Mechanics and*
980 *Mining Sciences*, 39(4), 429–442. doi: 10.1016/S1365-1609(02)00022-9

981 Rutter, E. (1983). Pressure solution in nature, theory and experiment. *Journal of*
982 *the Geological Society*, 140(5), 725–740. doi: 10.1144/gsjgs.140.5.072

983 Saffer, D. M., & Bekins, B. A. (1998). Episodic fluid flow in the Nankai accre-

984 tional complex: Timescale, geochemistry, flow rates, and fluid budget.
 985 *Journal of Geophysical Research: Solid Earth*, 103(B12), 30351–30370. doi:
 986 10.1029/98jb01983

987 Saffer, D. M., & Tobin, H. J. (2011). Hydrogeology and mechanics of subduction
 988 zone forearcs: Fluid flow and pore pressure. *Annual Review of Earth and Plan-
 989 etary Sciences*, 39, 157–186. doi: 10.1146/annurev-earth-040610-133408

990 Saffer, D. M., & Wallace, L. M. (2015). The frictional, hydrologic, metamorphic
 991 and thermal habitat of shallow slow earthquakes. *Nature Geoscience*, 8(8),
 992 594–600. doi: 10.1038/ngeo2490

993 Saishu, H., Okamoto, A., & Otsubo, M. (2017). Silica precipitation potentially con-
 994 trols earthquake recurrence in seismogenic zones. *Scientific reports*, 7(1), 1–10.
 995 doi: 10.1038/s41598-017-13597-5

996 Samuelson, J., Elsworth, D., & Marone, C. (2009). Shear-induced dilatancy of fluid-
 997 saturated faults: Experiment and theory. *Journal of Geophysical Research: Solid
 998 Earth*, 114(B12). doi: 10.1029/2008JB006273

999 Schmidt, W. L., & Platt, J. P. (2022). Stress, microstructure, and deformation
 1000 mechanisms during subduction underplating at the depth of tremor and slow
 1001 slip, Franciscan Complex, northern California. *Journal of Structural Geology*,
 1002 154, 104469. doi: 10.1016/j.jsg.2021.104469

1003 Schulz, R., Ray, N., Zech, S., Rupp, A., & Knabner, P. (2019). Beyond Kozeny–
 1004 Carman: predicting the permeability in porous media. *Transport in Porous
 1005 Media*, 130(2), 487–512. doi: 10.1007/s11242-019-01321-y

1006 Schwartz, S. Y., & Rokosky, J. M. (2007). Slow slip events and seismic tremor at
 1007 circum-Pacific subduction zones. *Reviews of Geophysics*, 45(3). doi: 10.1029/
 1008 2006RG000208

1009 Segall, P., & Bradley, A. M. (2012). Slow-slip evolves into megathrust earthquakes in
 1010 2D numerical simulations. *Geophysical Research Letters*, 39(18). doi: 10.1029/
 1011 2012GL052811

1012 Segall, P., & Rice, J. R. (1995). Dilatancy, compaction, and slip instability of a
 1013 fluid-infiltrated fault. *Journal of Geophysical Research: Solid Earth*, 100(B11),
 1014 22155–22171. doi: 10.1029/95JB02403

1015 Segall, P., Rubin, A. M., Bradley, A. M., & Rice, J. R. (2010). Dilatant strengthen-
 1016 ing as a mechanism for slow slip events. *Journal of Geophysical Research: Solid
 1017 Earth*, 115(B12). doi: 10.1029/2010JB007449

1018 Shelly, D. R., & Hardebeck, J. L. (2010). Precise tremor source locations and ampli-
 1019 tude variations along the lower-crustal central San Andreas Fault. *Geophysical
 1020 Research Letters*, 37(14). doi: 10.1029/2010GL043672

1021 Sibson, R. H. (1983). Continental fault structure and the shallow earth-
 1022 quake source. *Journal of the Geological Society*, 140(5), 741–767. doi:
 1023 10.1144/gsjgs.140.5.0741

1024 Sibson, R. H. (1992a). Fault-valve behavior and the hydrostatic-lithostatic fluid
 1025 pressure interface. *Earth-Science Reviews*, 32(1-2), 141–144. doi: 10.1016/0012
 1026 -8252(92)90019-P

1027 Sibson, R. H. (1992b). Implications of fault-valve behaviour for rupture nucleation
 1028 and recurrence. *Tectonophysics*, 211(1-4), 283–293. doi: 10.1016/0040-1951(92)
 1029 90065-E

1030 Sibson, R. H. (2000). Fluid involvement in normal faulting. *Journal of Geodynamics*,
 1031 29(3-5), 469–499. doi: 10.1016/S0264-3707(99)00042-3

1032 Sibson, R. H. (2017). Tensile overpressure compartments on low-angle thrust faults.
 1033 *Earth, Planets and Space*, 69(1), 1–15. doi: 10.1186/s40623-017-0699-y

1034 Sibson, R. H. (2020). Preparation zones for large crustal earthquakes consequent on
 1035 fault-valve action. *Earth, Planets and Space*, 72(1), 1–20. doi: 10.1186/s40623
 1036 -020-01153-x

1037 Skarbek, R. M., & Rempel, A. W. (2016). Dehydration-induced porosity waves and
 1038 episodic tremor and slip. *Geochemistry, Geophysics, Geosystems*, 17(2), 442–

1039 469. doi: 10.1002/2015GC006155

1040 Sleep, N. H., & Blanpied, M. L. (1992). Creep, compaction and the weak rheology of
1041 major faults. *Nature*, 359(6397), 687–692. doi: 10.1038/359687a0

1042 Sleep, N. H., & Blanpied, M. L. (1994). Ductile creep and compaction: A mecha-
1043 nism for transiently increasing fluid pressure in mostly sealed fault zones. *Pure*
1044 *and Applied Geophysics*, 143(1), 9–40. doi: 10.1007/BF00874322

1045 Suzuki, T., & Yamashita, T. (2009). Dynamic modeling of slow earthquakes based
1046 on thermoporoelastic effects and inelastic generation of pores. *Journal of Geo-
1047 physical Research: Solid Earth*, 114(B6). doi: 10.1029/2008JB006042

1048 Templeton, E. L., & Rice, J. R. (2008). Off-fault plasticity and earthquake rup-
1049 ture dynamics: 1. Dry materials or neglect of fluid pressure changes. *Journal of Geophysical
1050 Research: Solid Earth*, 113(B9). doi: 10.1029/2007JB005529

1051 Ujiie, K., Saishu, H., Fagereng, Å., Nishiyama, N., Otsubo, M., Masuyama, H., &
1052 Kagi, H. (2018). An explanation of episodic tremor and slow slip constrained
1053 by crack-seal veins and viscous shear in subduction mélange. *Geophysical
1054 Research Letters*, 45(11), 5371–5379. doi: 10.1029/2018GL078374

1055 Viesca, R. C., Templeton, E. L., & Rice, J. R. (2008). Off-fault plasticity and earth-
1056 quake rupture dynamics: 2. Effects of fluid saturation. *Journal of Geophysical
1057 Research: Solid Earth*, 113(B9). doi: 10.1029/2007JB005530

1058 Walder, J., & Nur, A. (1984). Porosity reduction and crustal pore pressure devel-
1059 opment. *Journal of Geophysical Research: Solid Earth*, 89(B13), 11539–11548.
1060 doi: 10.1029/JB089iB13p11539

1061 Wallace, L. M. (2020). Slow slip events in New Zealand. *Annual Review of Earth
1062 and Planetary Sciences*, 48, 175–203. doi: 10.1146/annurev-earth-071719
1063 -055104

1064 Wallace, L. M., Beavan, J., Bannister, S., & Williams, C. (2012). Simultaneous
1065 long-term and short-term slow slip events at the Hikurangi subduction margin,
1066 New Zealand: Implications for processes that control slow slip event occur-
1067 rence, duration, and migration. *Journal of Geophysical Research: Solid Earth*,
1068 117(B11). doi: 10.1029/2012JB009489

1069 Warren-Smith, E., Fry, B., Wallace, L., Chon, E., Henrys, S., Sheehan, A., ...
1070 Lebedev, S. (2019). Episodic stress and fluid pressure cycling in subduct-
1071 ing oceanic crust during slow slip. *Nature Geoscience*, 12(6), 475–481. doi:
1072 10.1038/s41561-019-0367-x

1073 Wibberley, C. A. (2002). Hydraulic diffusivity of fault gouge zones and implica-
1074 tions for thermal pressurization during seismic slip. *Earth, Planets and Space*,
1075 54(11), 1153–1171. doi: 10.1186/BF03353317

1076 Williams, R. T., & Fagereng, Å. (2022). The role of quartz cementation in the
1077 seismic cycle: a critical review. *Reviews of Geophysics*, 60(1), e2021RG000768.
1078 doi: 10.1029/2021RG000768

1079 Wood, D. M. (1990). *Soil behaviour and critical state soil mechanics*. Cambridge
1080 university press.

1081 Woodcock, N., & Mort, K. (2008). Classification of fault breccias and re-
1082 lated fault rocks. *Geological Magazine*, 145(3), 435–440. doi: 10.1017/
1083 S0016756808004883

1084 Xue, L., Brodsky, E. E., Erskine, J., Fulton, P. M., & Carter, R. (2016). A per-
1085 meability and compliance contrast measured hydrogeologically on the San
1086 Andreas Fault. *Geochemistry, Geophysics, Geosystems*, 17(3), 858–871. doi:
1087 10.1002/2015GC006167

1088 Xue, L., Li, H.-B., Brodsky, E. E., Xu, Z.-Q., Kano, Y., Wang, H., ... others
1089 (2013). Continuous permeability measurements record healing inside the
1090 Wenchuan earthquake fault zone. *Science*, 340(6140), 1555–1559. doi:
1091 10.1126/science.1237237

1092 Yang, Y., & Dunham, E. M. (2021). Effect of porosity and permeability evolution on
1093 injection-induced aseismic slip. *Journal of Geophysical Research: Solid Earth*,

1094 126(7), e2020JB021258. doi: 10.1029/2020JB021258

1095 Yarushina, V. M., Podladchikov, Y., & Wang, L. (2020). Model for (de) com-
1096 paction and porosity waves in porous rocks under shear stresses. *Journal*
1097 *of Geophysical Research: Solid Earth*, 125(8), e2020JB019683. doi:
1098 10.1029/2020JB019683

1099 Zhu, W., Allison, K. L., Dunham, E. M., & Yang, Y. (2020). Fault valving and pore
1100 pressure evolution in simulations of earthquake sequences and aseismic slip.
1101 *Nature communications*, 11(1), 1–11. doi: 10.1038/s41467-020-18598-z

1102 Zhu, W., David, C., & Wong, T. F. (1995). Network modeling of permeability evolu-
1103 tion during cementation and hot isostatic pressing. *Journal of Geophysical Re-*
1104 *search: Solid Earth*, 100(B8), 15451–15464. doi: 10.1029/95JB00958